Emission Features and Source Counts of Galaxies in Mid-Infrared

Cong Xu, Perry B. Hacking, Fan Fang, David L. Shupe, Carol J. Lonsdale, Nanyao Y. Lu, George Helou,

Infrared Processing and Analysis Center, Jet Propulsion Laboratory, Caltech 100-22, Pasadena, CA 91125

Gordon J. Stacey

Department of Astronomy, Cornell University, Ithaca, NY 14853

Matthew L. N. Ashby

Smithsonian Astrophysical Observatory

Optical & Infrared Astronomy Division

60 Garden Street MS 66, Cambridge, MA 02318

Received Jan. 12, 1998; accepted June 14, 1998

ABSTRACT

In this work we incorporate the newest ISO results on the mid-infrared spectral-energy-distributions (MIR SEDs) of galaxies into models for the number counts and redshift distributions of MIR surveys. A three-component model, with empirically determined MIR SED templates of (1) a cirrus/PDR component (2) a starburst component and (3) an AGN component, is developed for infrared (3–120 μm) SEDs of galaxies. The model includes a complete IRAS 25 μm selected sample of 1406 local galaxies ($z \leq 0.1$; Shupe et al. 1998a). Results based on these 1406 spectra show that the MIR emission features cause significant effects on the redshift dependence of the K-corrections for fluxes in the WIRE 25 μm band and ISOCAM 15 μm band. This in turn will affect deep counts and redshift distributions in these two bands, as shown by the predictions of two evolution models (a luminosity evolution model with $L \propto (1+z)^3$ and a density evolution model with $\rho \propto (1+z)^4$). The dips-and-bumps on curves of MIR number counts, caused by the emission features, should be useful indicators of evolution mode. The strong emission features at $\sim$ 6–8 μm will help the detections of relatively high redshift ($z \sim 2$) galaxies in MIR surveys. On the other hand, determinations of the evolutionary rate based on the slope of source counts, and studies on the large scale structures using the redshift distribution of MIR sources, will have to treat the effects of the MIR emission features carefully. We have also estimated a 15 μm local luminosity function from the predicted 15 μm fluxes of the 1406 galaxies using the bivariate (15 μm vs. 25 μm luminosities) method. This luminosity function will improve our understanding of the ISOCAM 15 μm surveys.

Subject headings: galaxies: starburst – Seyfert – luminosity function; infrared:

galaxies

1. Introduction

Current research on cosmology is focused on the debate whether the star formation history of the universe has a sharp peak in the redshift range of $z \sim 1 - 2$ (Madau *et al.* 1996), as derived from the Hubble Space Telescope deep surveys (Williams *et al.* 1996; Griffiths *et al.* 1994) and from ground based redshift surveys (Lilly *et al.* 1995; Koo and Kron 1992), or the universe had been forming stars in a relatively constant rate since an early galaxy formation time ($z \sim 5$) until $z \sim 1$ (Franceschini *et al.* 1997; Rowan-Robinson *et al.* 1997), as suggested by the cosmic far-infrared (FIR) background studies (Puget *et al.* 1996; Guiderdoni *et al.* 1997) and studies on the metal abundance in Intra-Cluster Medium (Mushotzky and Loewenstein 1997).

The problem with the HST surveys and ground based redshift surveys is the dust extinction, which may hide much of the star formation in early universe from these UV/optical surveys. Dust extinction has little effect on mid-infrared (MIR, 4 μm— 40 μm) surveys. Compared to the FIR (>40 μm) deep surveys, the MIR surveys also have the advantage of using larger detector arrays and having better resolutions; the latter is of particular importance because in these bands the depth of a survey is ultimately constrained by the confusion limit. Therefore, MIR surveys will play important roles in galaxy evolution studies. Indeed, currently several deep MIR surveys are either being carried out using ISO (Franceschini *et al.* 1996; Oliver *et al.* 1997), or soon to be launched such as WIRE (Hacking *et al.* 1996; Schember *et al.* 1996) and SIRTF (Cruikshank and Werner 1997).

On the other hand, it was known before ISO that in the wavelength range between 3–20 μm there are several broad band features (see Puget and Léger 1989 for a review), which may contribute substantially to the IRAS 12 μm flux of galaxies (Gillett *et al.* 1975; Phillips *et al.* 1984; Giard *et al.* 1989; Helou *et al.* 1991). The best candidates for the emitters of these features are some large molecules (~1 nm) of Polycyclic Aromatic

Hydrocarbon (Léger and Puget 1984; Allamandola *et al.* 1985), and the features are often called PAH features. New ISO observations (Lu *et al.* 1996, 1998; Vigroux *et al.* 1996; Boulade *et al.* 1996) show further that these features are present in the MIR spectra of most galaxies, and their equivalent widths can be as large as $\sim$10 μm, comparable to or even larger than typical band passes for MIR filters (e.g. the band pass of the ISOCAM 15 μm filter is $\sim$6 μm). This indicates that when any of these features moves in or out of the band pass of a MIR survey, because of the redshifts of galaxies, very significant K-corrections will occur. Interpretations of MIR survey counts have to take this fact into account. A pre-ISO attempt on this issue, based on the laboratory PAH spectra (instead of the spectra of galaxies), can be found in Maffei (1994).

It is the primary aim of this paper to develop a new, emiprical model for the MIR SED's of galaxies, and incorprate it into the model for number counts of MIR surveys. The SED model is built upon available MIR spectra of galaxies taken from published ISO observations, and is applied to the 1406 galaxies (with $z < 0.1$) of the 25 μm sample of Shupe *et al.* (1998a), selected from the IRAS Faint Point Source Catalog (Moshir *et al.* 1992). For each galaxy in the sample a model spectrum is obtained, which has the MIR emission features and which can reproduce the four observed IRAS fluxes. These 1406 spectra are used to determine the K-corrections and their dispersions in our model for predictions on number counts and redshift distributions of MIR surveys. The effects of the emission features on these predictions are investigated. Detailed comparisons of the model results with some ISOCAM MIR surveys (Oliver *et al.* 1997; Clements *et al.* 1998) and predictions for WIRE survey will be found in a separate paper (Hacking et al. 1998). The computer code of the model presented here is available upon request to CX.

The paper is arranged as follows: the SED model is developed in Section 2. A local luminosity function at 15 μm, calculated from the predicted 15 μm fluxes of the 1406

galaxies, is presented in section 3. In Section 4 we present the model for source counts and investigate the effects of the emission features on the MIR number counts. Section 5 is devoted to the discussion and Section 6 to the conclusion.

2. An empirical model for IR SEDs of galaxies

2.1. Properties of MIR SEDs of galaxies

The following properties of MIR SEDs of galaxies can be found from the literature:

1. The MIR SEDs of normal galaxies (without AGNs) in the ~10 μm region are not smooth. Indeed there has been evidence for this since the observations of Gillett *et al.* (1975) of the 8–13 μm spectra of M 82 and NGC 253, the two nearby prototype starburst galaxies. Later ground-based observations (Roche *et al.* 1991) and the IRAS low-resolution spectral observations (Cohen and Klein 1989) show further that the 11.3 μm feature and the 8 μm feature are very common in the 8 – 13 μm spectra of 'HII' galaxies (i.e. starburst galaxies). Most recently, Lu *et al.* (1996, 1998) obtained MIR spectra (3–11.7 μm) of a sample of late-type galaxies using ISO. These galaxies are part of a larger set of star-forming galaxies, selected to cover a broad range of infrared and optical properties, in the ISO key project on normal galaxies (Helou *et al.* 1996). The spectra were taken with ISOPHT operated in its PHT-S spectroscopic mode (Lemke *et al.* 1996) with a triangular chopping on both sides of the galaxy on the sky. In the wavelength range covered by the observations, 3–11.7 μm, several prominent broad band features (e.g. at 6.2 μm, 7.7 μm, 8.6 μm and 11.3 μm) are clearly visible in almost every spectrum in the sample. ISOCAM CVF spectrum of NGC 5195 (the small companion of M51) shows further that beyond the PHT-S long wavelength boundary there is still another broad feature at ~12.7 μm (close to the

[NII] line at 12.8 μm; Boulade *et al.* 1996). All of these features are presumably emission bands of PAH molecules corresponding to different C-C and C-H modes (Léger and Puget 1984; Allamandola *et al.* 1985).

2. Viewing through the gallery of ISO MIR spectra of galaxies (Lu *et al.* 1996, 1998; Boulade *et al.* 1996; Vigroux *et al.* 1996; Metcalfe *et al.* 1996; Acosta-Pulido *et al.* 1996), of Galactic star formation regions and reflection nebulae (Verstraete *et al.* 1996; Cesarsky *et al.* 1996a, 1996b; Boulanger *et al.* 1996), and of Galactic cirrus (Mattila *et al.* 1996), it appears that in general, the PAH features and the underlying continuum in the MIR band correlate tightly, indicating that they may have the same origin. Except for the HII regions and violent starburst regions in interacting galaxies, the shape of the MIR spectra of galaxies, of different Galactic nebulae and of Galactic cirrus are remarkably similar. However, in the core of Galactic HII regions (Cesarsky *et al.* 1996b; Verstraete *et al.* 1996) and in a violent starburst region in Arp 244 (the famous Antennae which is a local example of galaxy merger), another component of the continuum which increases sharply with wavelength appears (Cesarsky *et al.* 1996b; Vigroux *et al.* 1996; Verstraete *et al.* 1996). In the framework of the dust model of Désert et al. (1990), this latter component is likely to be due to the 3-dimensional very small grains heated by the combined heating of multiple photons (Boulanger *et al.* 1996). The characteristic temperature of this component is usually too low for it to be seen at wavelengths <20 μm when the heating radiation intensity is below $\sim 10^4$ times the local ISRF (Cesarsky *et al.* 1996b). Noticeably, this component affects mostly the MIR emission at $\lambda > 12$ μm and not so much for the emission at shorter wavelengths as shown by the ISO PHT-S spectra (3 – 11.7 μm) of galaxies in the sample of Lu *et al.* (1998) which includes both quiescent and starburst galaxies.

3. From their ground based observations Roche *et al.* (1991, see also Moorwood 1986) found that many active galactic nuclei (AGNs) show distinctively different MIR spectra from those of starburst galaxies, in particular the broad band emission features are absent. This is confirmed by new ISO observations (e.g. Lutz *et al.* 1997a; Genzel *et al.* 1998). Roche *et al.* (1991) argued that it is the AGN itself, instead of other reasons such as the abundance of certain elements, that affects the dust emission process to suppress the MIR features either by alternating the grain composition within the nuclear region, perhaps by the selective destruction of grain species, or through very different excitation conditions.

2.2. Our model

Our model is based on the following assumptions:

Assumption 1: The MIR SED (3–16 μm) of galaxies has three components, each has a fixed SED given by the corresponding template (Figures 1–3): (1) a cirrus/PDR (Photo-Dissociation Region) component which is dominant in the MIR SEDs of most of normal galaxies, (2) a starburst component due to dust heated by the very intense radiation in starburst regions which is likely to be the dominant component for violent starburst galaxies such as Arp 220, and (3) an AGN component due to the dust emission associated with AGNs.

The adopted MIR spectrum (3–16 μm) of the cirrus/PDR component is presented in Figure 1 (the solid curve). Lu *et al.* (1998) gives two average spectra, one from a set of 10 "FIR-cold" galaxies with an IRAS 60 μm–to–100 μm flux density ratio, $f_{60\mu}/f_{100\mu}$, between 0.28 and 0.40; and one from a set of 9 "FIR-warm" galaxies with $0.60 < f_{60\mu}/f_{100\mu} < 0.88$. The relative flux accuracy of these spectra should be good to about 20%. The shape of our

cirrus/PDR template spectrum at wavelengths shorter than ~12 μm is identical to that of the average spectrum for the FIR-cold galaxies in Lu *et al.* (1998). At longer wavelengths a tail is taken from the spectrum of NGC 5195 (Boulade *et al.* 1996). It can be seen that the two spectra agree reasonably well at the wavelengths covered by both.

In the wavelength range of 8.7–16 μm the spectrum of the starburst component (Figure 2) is taken from the ISO-CAM CVF spectrum of the overlapping region (region A) in Arp 244 (Vigroux *et al.* 1996), the famous Antennae. This region is where the two disks crash, and where much of the star formation in this merging system is taking place. The emission features are still visible in the spectrum, but most of the energy is in the continuum which has a relatively steep slope. Shorter than 8.7 μm, the shape of the spectrum of region A in Arp 244 is very close to that of the average spectrum for the FIR-warm galaxies in Lu *et al.* (1998). Therefore shorter than 8.7 μm the starburst component is taken from the latter (Fig.2) which extends to 3 μm. Interestingly, longer than 8.7 μm the MIR continuum in the average spectrum of the FIR-warm galaxies of Lu *et al.* is not as strong as in the starburst region in Arp 244, suggesting that in these galaxies a significant fraction of the MIR emission is emitted outside the starburst regions (i.e. associated with the cirrus/PDR component).

It should be noted that in the short wavelength channel of ISOPHT-S (<5 μm) the mean spectra of Lu *et al.* (1998) are rather noisy, and show no significant evidence for any detection of features (e.g. the 3.3 μm feature) at $\lambda < 5$ μm. Thus both cirrus/PDR template and the starburst template presented above are approximated by flat spectra in the wavelength range 3 μm $< \lambda < 5$ μm, determined by the average flux densities (over the same wavelength range) of the mean spectrum of the FIR-cold galaxies and of the mean spectrum of the FIR-warm galaxies of Lu *et al.* (1998), respectively.

The template of the MIR SED of the AGN component (Figure 3) is based on the MIR

spectrum of the Seyfert 2 nucleus of NGC 1068 (Lutz *et al.* 1997a). Because we are only interested in the broad band SED, the narrow emission lines in this wavelength range are not included.

Assumption 2: For a given galaxy with measured IRAS fluxes of $f_{25\mu}$ and $f_{60\mu}$, the 25 μm flux of the AGN component can be determined using the following 'color-method':

$$\mathrm{f}_{25\mu}^{\mathrm{AGN}} = \begin{cases} f_{25\mu} & (\mathrm{f}_{60\mu}/\mathrm{f}_{25\mu} \leq 2.5); \\ f_{25\mu} \times \frac{5-f_{60\mu}/f_{25\mu}}{5-2.5} & (2.5 < \mathrm{f}_{60\mu}/\mathrm{f}_{25\mu} < 5); \\ 0 & (\mathrm{f}_{60\mu}/\mathrm{f}_{25\mu} \geq 5). \end{cases} \quad (1)$$

This assumption is based on the fact that galaxies with low $f_{60\mu}/f_{25\mu}$ ratios have a large chance of exhibiting Seyfert activity (de Grijp *et al.* 1985). In an optical spectroscopic survey for a FIR color selected sample of 358 extragalactic sources with $1 < f_{60\mu}/f_{25\mu} < 3.72$ (i.e. $-1.5 < \alpha_{25,60} < 0$), Keel *et al.* (1994) found that more than 60 percent of the sources are Active galaxies (including Seyferts, QSOs and BL Lacs). In Figure 4 is plotted the $f_{25\mu}/f_{12\mu}$ vs. $f_{25\mu}/f_{60\mu}$ color-color diagram of the IRAS 25 μm selected sample of Shupe *et al.* (1998a). Sources with known AGNs (identified using NED) are plotted with different symbols. Indeed we find that for $\log(f_{25\mu}/f_{60\mu}) \geq -0.4$ (i.e. $f_{60\mu}/f_{25\mu} \leq 2.5$) the vast majority of the sources are Active galaxies. In particular, most of the QSOs are on the right side of this boundary. On the other hand, most of the normal galaxies (i.e. without AGN) have $\log(f_{25\mu}/f_{60\mu}) \leq -0.3$ (i.e. $f_{60\mu}/f_{25\mu} \geq 5$). Interestingly, many galaxies with AGNs, in particular most of the LINERs, also have $\log(f_{25\mu}/f_{60\mu}) \leq -0.3$. It is likely that for these sources the IR fluxes are mainly from the host galaxies and the AGN component is not significant.

Once $f_{25\mu}^{AGN}$ is determined, the 12 μm flux of the AGN component is derived as follows:

$$\mathrm{f}_{12\mu}^{\mathrm{AGN}} = \begin{cases} 0.6\, f_{25\mu}^{AGN} & (\mathrm{f}_{25\mu}^{\mathrm{AGN}} < \mathrm{f}_{25\mu} \text{ and } 0.6\, \mathrm{f}_{25\mu}^{\mathrm{AGN}} < \mathrm{f}_{12\mu}) \\ f_{12\mu} & (\text{otherwise}) \end{cases} \quad (2)$$

The standard $f_{12\mu}/f_{25\mu}$ ratio of 0.6 for the AGN component is taken from that of the Seyfert 2 nucleus of NGC 1068 (Lutz 1997a).

Based on the IRAS data, Giuricin *et al.* (1995) found that Seyfert 2 galaxies tend to have steeper continuum spectra between 12 and 25 μm than those of Seyfert 1 galaxies. However, given the large beams of IRAS detectors, it is not clear whether this reflects the intrinsic difference between the two types of AGN or whether it is due to the difference in the star formation activity around Seyfert 1s and Seyfert 2s (Maiolino *et al.* 1995). In this work, we choose to use a single template (Figure 3) to model the MIR SED of both types of AGN.

Assumption 3: Define

$$\mathrm{f}^{\mathrm{G}}_{25\mu} = \mathrm{f}_{25\mu} - \mathrm{f}^{\mathrm{AGN}}_{25\mu} \tag{3}$$

and

$$\mathrm{f}^{\mathrm{G}}_{12\mu} = \mathrm{f}_{12\mu} - \mathrm{f}^{\mathrm{AGN}}_{12\mu} \quad . \tag{4}$$

The 12 μm fluxes of the starburst component and of the cirrus/PDR component can be determined by the color $f^G_{25\mu}/f^G_{12\mu}$ through the following formulae:

$$\mathrm{f}^{\mathrm{SB}}_{12\mu} = \begin{cases} f^G_{12\mu} & (f^G_{25\mu}/f^G_{12\mu} \geq 6); \\ \frac{f^G_{25\mu}/f^G_{12\mu}-2}{6-2} & (2 < \mathrm{f}^{\mathrm{G}}_{25\mu}/\mathrm{f}^{\mathrm{G}}_{12\mu} < 6); \\ 0 & (f^G_{25\mu}/f^G_{12\mu} \leq 2) \end{cases} \tag{5}$$

and

$$\mathrm{f}^{\mathrm{PDR}}_{12\mu} = \mathrm{f}^{\mathrm{G}}_{12\mu} - \mathrm{f}^{\mathrm{SB}}_{12\mu}. \tag{6}$$

In this assumption, we assign a significantly higher standard $f_{25\mu}/f_{12\mu}$ color ratio to the starburst component ($f^{SB}_{25\mu}/f^{SB}_{12\mu} = 6$) than that of the cirrus/PDR component

($f_{25\mu}^{PDR}/f_{12\mu}^{PDR} = 2$), to be consistent with the fast-rising MIR SED of the starburst template (Figure 2). This is also consistent with the anti-correlation between $f_{12\mu}/f_{25\mu}$ and $f_{60\mu}/f_{100\mu}$ of galaxies (Helou 1986) given that the $f_{60\mu}/f_{100\mu}$ ratio is a good star formation strength indicator (Bothun *et al.* 1989; Xu and De Zotti 1989). For example Arp 299 (NGC 3690/IC 694), a famous local example of galaxy mergers, has $f_{25\mu}/f_{12\mu} = 5.8$ and $f_{60\mu}/f_{100\mu} = 0.95$.

Given Equations 1, 2, 5, and 6, we can calculate the 12 μm fluxes of the three components for a given galaxy with measured $f_{12\mu}$, $f_{25\mu}$ and $f_{60\mu}$. These 12 μm fluxes provide the absolute calibrations for the MIR SED templates of these components, the sum of which is the model MIR SED (3–16 μm) for the galaxy in question.

Assumption 4 There are no broad band features at wavelengths longer than 16 μm in the IR emission of galaxies.

This assumption is based on the available IR spectra in the literature. In particular the ISOSWS spectrum of M 82 (Lutz *et al.* 1997b), which covers the wavelength range 3–40 μm, does not show any broad band features beyond the 12.7 μm feature. Consequently, for a given galaxy, the IR radiation spectrum at wavelengths longer than 16 μm is determined in our SED model by fitting the 3 IRAS fluxes at 25, 60 and 100 μm (taking into account the real responsivity functions of IRAS detectors), and the flux density at 16 μm predicted by the sum of the three MIR components, using a simple cubic spline algorithm (obviously the continuum so determined joins at 16 μm the model MIR SED). The advantage of this empirical model is that it preserves the observed flux measurements of each source and allows the inclusion of a large sample of galaxies in a wide range of observed SEDs.

Figure 5 is a flow chart showing how actually our model proceeds.

2.3. Tests of the SED model

In Figure 6 the predicted MIR spectrum of M 82 and the observed ISOSWS spectrum of M 82 (Lutz *et al.* 1997b) are compared. Allowing for the small apertures of ISOSWS channels (ranging from $14'' \times 20''$ to $17'' \times 40''$), we have multiplied the IRAS fluxes of M 82 at 12, 25, 60, and 100 μm by 0.38, 0.5, 0.5 and 0.38, respectively. Admittedly these factors are somewhat arbitrary because at these wavelengths no high resolution maps of M 82 are available for us to do aperture photometry. So they are chosen to give the best fit. Nevertheless they look reasonable. In particular, the two different factors (0.5 for $f_{25\mu}$and $f_{60\mu}$, 0.38 for $f_{12\mu}$ and $f_{100\mu}$) can be understood by means of the known anti-correlation in the $f_{12\mu}/f_{25\mu}$ vs. $f_{60\mu}/f_{100\mu}$ diagram (Helou 1986), which suggests that $f_{25\mu}$and $f_{60\mu}$ are more concentrated in the starburst nucleus of M 82. The good agreement between the predicted and observed MIR *continuum* is indeed due to the fine tuning of the aperture corrections, while the good agreements between the shapes of the MIR *features* (which are independent of the fitting of the continuum) on the predicted and observed spectra are truly remarkable.

We made a further test to determine whether the model reliably predicts galaxies' MIR SEDs. Ashby *et al.* (1999) observed with ISOPHT-P a sample of 29 FIR bright galaxies ($f_{60\mu} > 5.8$ Jy) in several MIR wavelength bands, including the PHT-P 16 μm band ($52''$ aperture). Our SED model was applied to a subsample of 18 of the Ashby *et al.* galaxies. The subsample was selected based on four criteria: (1) the signal-to-noise ratio of the PHT-P 16 μm flux > 3; (2) detection of the galaxy by IRAS in both the 12 and 25 μm bands; (3) optical extent $< 2'$, or when in a galaxy pair the combined size of the pair is $< 2'$, (4) the distance to the nearest neighbor (of similar optical brightness) $> 4'$. The last two criteria ensure that the PHT-P observations include most of the emission from the region enclosed in the IRAS apertures ($\sim 4'$). Convolving the predicted spectra with the

PHT-P 16 μm responsivity function, the 16 μm fluxes are predicted and compared with the observed $f_{16\mu}$ (Figure 7). Given the uncertainty of the observed $f_{16\mu}$ (in most case $\sim$ 30%, Ashby et al. 1999), the agreement between the predicted and observed $f_{16\mu}$'s is quite good. The model spectra of the same galaxies are plotted in Figure 8.

2.4. The Sample

The IRAS 25 μm selected sample (complete down to $f_{25\mu} = 0.25$ Jy) of Shupe *et al.* (1998a) contains 1458 galaxies, all have measured redshifts and measured IRAS 25 μm fluxes. In order to have a local sample free from significant evolutionary effects, our sample includes only the 1406 galaxies in Shupe et al's sample which have redshifts ≤ 0.1. Most of them are also detected by IRAS at 12, 60 and 100 μm. At 12 μm, 330 (out of 1406) galaxies are not detected by IRAS and have therefore only upper limits. For $f_{60\mu}$ and $f_{100\mu}$, 18 and 94 galaxies have upper limits, respectively. We assign a flux density $f_\nu = 0.8\times$upper limit for these cases.

The SED model thus produces for each galaxy in the sample a SED from 3–120 μm. As examples, the SEDs of 50 galaxies with $9 \leq \log(\nu L_\nu(25\mu\mathrm{m})/L_\odot) \leq 10$ are plotted in Figure 9.

3. Local luminosity function at 15 μm

Several MIR surveys (Oliver *et al.* 1997; Franceschini *et al.* 1996) are being carried out by ISOCAM in the 15 μm band, the most sensitive one for starburst galaxies among ISOCAM filters. However, there is no 15 μm local luminosity function (LLF) available in the literature, because there have been no complete samples of galaxies in 15 μm band. Oliver *et al.* (1997) used the 12 μm LLF of Rush et al. (1993) in the interpretation of

their 15 μm deep survey. This may be problematic because different galaxies have different 15-to-12 μm flux ratios.

We construct a 15 μm LLF in this section exploiting the model SEDs of the 1406 galaxies in our sample. First, for each galaxy in the sample, an in-band flux at 15 μm is derived by convolving its SED with the responsivity functions of ISOCAM 15 μm filter (13–18 μm, ISOCAM User's Manual). The monochromatic flux at 15 μm is derived from this by assuming νf_ν =constant within the bandpass. When there is only an upper limit at 12 μm, instead of multiplying a by factor of 0.8 to get an approximation of the real flux as in the previous section, here we input the 12 μm upper limit into the SED model and obtain an upper limit for the 15 μm flux. The 15 μm LLF can then be calculated from the predicted 15 μm luminosities, and the corresponding upper limits, of these galaxies.

Since our sample is 25 μm-flux limited, not 15 μm-flux limited, the bivariate method is used in the calculation of the 15 μm luminosity function. The basic formula is

$$\Psi(L_{15\mu} > l_{15\mu}) = \int \Theta(L_{15\mu} > l_{15\mu}|L_{25\mu})\ \rho(L_{25\mu})\ \ d\,L_{25\mu} \tag{7}$$

here Ψ is the 15 μm *integral* luminosity function, ρ the 25 μm *differential* luminosity function (Shupe *et al.* 1998a), and Θ the conditional probability function for a galaxy with given 25 μm luminosity $L_{25\mu}$ to have the 15μ luminosity $L_{15\mu}$ brighter than $l_{15\mu}$. The integration is over the entire range of the 25 μm luminosity. The derivative of Ψ gives the differential luminosity function:

$$\phi(L_{15\mu}) = \int \frac{\partial\Theta}{\partial L_{15\mu}}\rho(L_{25\mu})\ \ d\,L_{25\mu}\ . \tag{8}$$

In practice, the luminosity functions are calculated in the domain of the logarithms of the luminosities. Hence the $L_{15\mu}$'s and the $L_{25\mu}$'s in above formulae should be replaced by the corresponding logarithms. The sample is binned for both $\log(L_{25\mu})$ and $\log(L_{15\mu})$, and

Eq(8) can be approximated by

$$\phi[\log(L_{15\mu}) = L_i] = \sum_j P_{i,j}\rho[\log(L_{25\mu}) = L_j]\ \ \Delta_j/\delta_i \tag{9}$$

where L_j and Δ_j are the center and the width of the j-th bin of $\log(L_{25\mu})$, L_i and δ_i are the center and the width of the i-th bin of $\log(L_{15\mu})$, and $P_{i,j}$ is the probability of galaxies in the j-th bin of $\log(L_{25\mu})$ (i.e. $L_j - 0.5\Delta_j \leq log(L_{25\mu}) < L_j + 0.5\Delta_j$) to have $\log(L_{15\mu})$ in the bin L_i ($L_i - 0.5\delta_i \leq \log(L_{15\mu}) < L_i + 0.5\delta_i$).

In order to take into account the information contained in the upper limits, the Kaplan-Meier estimator (Kaplan and Meier 1958) is applied in the calculation of $P_{i,j}$ and its variance. In what follows we give a brief description of the algorithm.

For the subsample of galaxies in the j-th bin of $\log(L_{25\mu})$, define F_{i-1} as the probability function

$$F_{i-1} = P[\log(L_{15\mu}) < L_i + 0.5\delta_i] \tag{10}$$

and

$$F_i = P[\log(L_{15\mu}) < L_i - 0.5\delta_i]\ . \tag{11}$$

So,

$$P_{i,j} = F_{i-1} - F_i \tag{12}$$

and

$$Var(P_{i,j}) = Var(F_{i-1}) + Var(F_i) - 2 \times Covar(F_{i-1}, F_i)\ . \tag{13}$$

The algorithm for calculating the KM estimator of $F_{i-1}, F_i, Var(F_{i-1})$ and $Var(F_i)$ can be found in Feigelson and Nelson (1985), while the KM estimator for the covariance between F_{i-1}, F_i (for $F_i > 0$) is (Akritas and LaValley 1997)

$$Covar(F_{i-1}, F_i) = \frac{F_{i-1}}{F_i} Var(F_i)\ . \tag{14}$$

Finally, the variance of ϕ is

$$Var[\phi(\log(L_{15\mu}) = L_i)] = \sum_j \{ \quad Var(P_{i,j})\rho[\log(L_{25\mu}) = L_j] + P_{i,j} Var[\rho(\log(L_{25\mu}) = L_j)]\}(\Delta_j/\delta_i)^2 \, . \tag{15}$$

The resultant 15 μm differential luminosity function is given in Table 1 and plotted in Figure 10. A least-squares fit to the *integral* 15 μm luminosity function by a smooth function with the form (Yahil *et al.* 1991)

$$\Psi(L) = C \left(\frac{L}{L_\star}\right)^{-\alpha} \left(\frac{1+L}{L_\star}\right)^{-\beta} \tag{16}$$

is carried out. The parameters of this fitting function are given in Table 2. The *differential* 15 μm luminosity function specified by these parameters is given in Figure 10 by the solid line.

4. MIR number counts model and effects of emission features

4.1. Model for number counts

Our model for galaxy counts as a function of the limiting MIR flux and redshift follows the prescription of Condon (1984; see also Hacking *et al.* 1987; Hacking & Soifer 1991). Here we give a brief outline of the formulation. Details can be found in the above references.

We consider only one set of cosmological parameters, namely $H_0 = 75$, $\Omega = 1$ ($q = 0.5$), and the cosmological constant $\Lambda = 0$.

Let $\rho(L)$ be the local differential luminosity function (number of galaxies in unit comoving volume and unit $\log(L)$ interval). When the evolutionary effects are taken into account, the LF at redshift z is

$$\rho'(L, z) = G(z)\, \rho\left(\frac{L}{F(z)}\right); \tag{17}$$

where $G(z)$ is the density evolution function and $F(z)$ the luminosity evolution function.

The monochromatic luminosity in the rest frame is:

$$L_\nu = f_\nu 4\pi D_L^2 \times 10^{0.4K}, \tag{18}$$

where f_ν (hereafter f) is the observed flux density, z the redshift, D_L the luminosity distance:

$$D_L = \frac{2c}{H_0}(1+z)[1-(1+z)^{-0.5}] \ , \tag{19}$$

and K the standard K-correction (Lang 1980):

$$K = 2.5\log(1+z) + 2.5\log\frac{\int_{\lambda_1}^{\lambda_2} S(\lambda)R(\lambda)\,d\lambda}{\int_{\lambda_1}^{\lambda_2} S(\lambda/(1+z))R(\lambda)\,d\lambda} \ . \tag{20}$$

The derivative of the comoving volume vs. redshift z is

$$\begin{aligned}\frac{dV}{dz} &= 4\pi D_A^2 \ \frac{d\,D_A}{d\,z} \\ &= 4\pi D_A^2 \ \frac{c}{H_0(1+z)^{1.5}} \ .\end{aligned} \tag{21}$$

where D_A is the angular distance:

$$D_A = \frac{2c[1-(1+z)^{-0.5}]}{H_0} \ . \tag{22}$$

By definition the K-correction is a function of the redshift. However, for a given bandpass ($R(\lambda)$), the K correction also depends on the detailed spectrum ($S(\lambda)$), which varies from galaxy to galaxy. Therefore for the model it is more appropriate to define the K-correction as a random variable with its *probability distribution* depending on the redshift and on some other observables. Our prescription for the K-correction explicitly includes a luminosity dependence because IRAS data have shown that the $f_{12\mu}/f_{25\mu}$ color (and therefore the MIR SED) is a strong function of the MIR luminosity (Fang *et al.* 1998). In this work we choose to approximate the K distribution by a Gaussian:

$$U(K,L,z) = \frac{1}{\sqrt{2\pi}\sigma_K} \ \exp\frac{-(K-K_0)^2}{2\sigma_K^2} \tag{23}$$

where the mean K_0 and the dispersion σ_K are dependent on the *luminosity* L and the redshift z. We have also tried a prescription where the K-correction is a function of the FIR-to-blue luminosity ratio instead of the MIR luminosity L. No significant changes are found in the results for the number counts.

Given the above definitions, we have:

$$\eta(L,z,K)\; d\log(L)\; dz\; dK = \rho'(L,z)\; U(K,L,z)\; \frac{dV}{dz}\; d\log(L)\; dz\; dK \qquad (24)$$

where η is the counts per unit $\log(L)$ interval per unit z interval per unit K interval. Substituting the variable L by f according to Eq(18) for given z and K, and integrating over K, one obtains the prediction for the differential counts per unit $\log(f)$ interval and per unit z interval:

$$\xi(f,z) = \int_{-\infty}^{\infty} \rho'[(L(f,z,K),z]\; U[K,L(f,z,K),z]\frac{dV}{dz}\; dK \quad . \qquad (25)$$

4.2. K-corrections

The narrower the bandpass[1], the more significant the effect of the emission features on the K-correction. Here we compare the predicted K-corrections for three bandpasses: ISOCAM 12 μm band, ISOCAM 15 μm band (ISOCAM User's Manual), and WIRE 25 μm band (Shupe et al. 1998b). The responsivity of these filters are plotted in Figure 11.

For each of the three bands, K-corrections at different z are calculated for each of the 1406 galaxies in our sample using its model spectrum and Eq(20). Then the sample is binned according to the monochromatic luminosity (rest frame) at the effective wavelength of the band, and the means and the dispersions of the K-corrections at different z are

[1]The width of a bandpass is better defined by $log(\lambda_2) - log(\lambda_1)$, which is not affected by the redshift.

calculated for the subsample of galaxies in each bin, which are used as estimators of the $K_0(L,z)$ and $\sigma_K(L,z)$ in Eq(23).

In Figures 12a, 12b and 12c the mean K_0 as function of redshift z for galaxies with different luminosities are plotted for the three filters, respectively, and the dispersions σ_K are plotted as error bars. And in Figures 12d, 12e and 12f, the dependences of K_0 and σ_K on luminosity are plotted for $z = 0.5$, $z = 1$ and $z = 2$ for the same filters. The K-z curves for WIRE 25 μm band flux demonstrate two dips near $z = 1$ and $z = 2$, which are due to the MIR emission features at $\sim$ 11–12 μm and at $\sim$ 6–8 μm (see Figures 1 and 2), respectively. The peak around $z = 1.5$ is caused by the trough at $\sim$ 9–10 μm in MIR SEDs of galaxies, which may partially be due to the silicate absorption. For the ISOCAM 15 μm band flux, the bump caused by this SED trough moves to $z \sim 0.5$ and the emission features at 7–8 μm cause a dip around $z = 1$. The K-z curves for the ISOCAM 12 μm band (the most broad band among the three) are relatively smooth.

4.3. Number counts

Through K-corrections, the MIR features affect the number counts and the redshift distributions of deep surveys. Figures 13a, 13b and 13c show Euclidean normalized differential counts predicted by different models of the cosmological evolution of galaxies for ISOCAM 12 μm, ISOCAM 15 μm and WIRE 25 μm bands. The $L \propto (1+z)^3$ model is chosen because it fits the IRAS 60 μm counts (Pearson and Rowan-Robinson 1996) well, and the results from the $\rho \propto (1+z)^4$ model are presented to highlight the difference between a density evolution model and a luminosity evolution model. The latest local luminosity functions (LLFs) at 12 μm (Fang *et al.* 1998) and 25 μm (Shupe *et al.* 1998a) which improve upon the earlier LLFs in these bands (Soifer and Neugebauer 1991; Rush *et al.* 1993), and the 15 μm LLF presented in Section 3 are used in the calculations of model

predictions.

In order to demonstrate the effects of the MIR features on the number counts, in Figures 13d, 13e and 13f we show the Euclidean normalized differential counts predicted by evolution models based on model spectra of galaxies **without** the MIR features, which are calculated using the smooth fits (power-laws) of the templates of the three components in Section 2.

In all of the three bands considered, the effects of the MIR features on the number counts predicted by the density evolution model ($\rho \propto (1+z)^4$) are significant. In Figures 13d, 13e, and 13f (no MIR features) the curves of predicted number counts by the density evolution model are rather flat, while in Figures 13a, 13b, and 13c the corresponding curves show dips and bumps caused by the MIR features. For example in Figure 13b (15 μm) the curve of number counts predicted by the density evolution model shows two shallow bumps which are due to the emission features in the 11–13 μm wavelength range and those in the 6–8.5 μm wavelength range, respectively. The prominent bump at $f_{25\mu} \sim 0.1$ mJy in Figure 13c (25 μm) is due to the features in both the 6–8.5 μm wavelength range and the 11–13 μm wavelength range (see the discussion of Figure 14). It appears that in all three bands the MIR features cause only slight distortions on the number counts predicted by the no evolution models.

There is a broad peak on the number counts predicted by the luminosity evolution model ($L \propto (1+z)^3$) in all six panels including those for models without the emission features. Hence this peak is not due to the emission features. Instead it is a combined effect caused by other two factors, one related to the evolutionary model and the other to the adopted cosmological model ($q_0 = 0.5$): The strong evolution ($L \propto (1+z)^3$) ensures that before the depth of a survey getting close to the 'edge' of the visible universe (i.e. $z \lesssim 1$) the number counts increase much faster than the Euclidean predictions. Then,

when the flux level becomes so faint that the characteristic redshifts of galaxies are significantly larger than unity (for a given flux, the stronger the luminosity evolution, the larger the characteristic redshift), the slope of dV/dz (Eq(21)) starts to decrease rapidly with increasing z (decreasing flux), and the number counts drop significantly below the Euclidean predictions.

The effects of the MIR features on the number counts predicted by the luminosity evolution model look moderate. The peaks in Figure 13a (12 μm) and in Figure 13b (15 μm) are slightly narrower than those in Figure 13d and Figure 13e, and the peak in Figure 13c (25 μm) is slightly broader than that in Figure 13f.

In Figures 14a–f, we compare the redshift distributions of sources at the flux level of $f_\nu = 0.5$ mJy, predicted by different evolutionary models. Note that these distributions are for galaxies **at** this flux level, rather than for galaxies in samples brighter than this flux. The flux $f_\nu = 0.5$ mJy is about the location of the peaks on the predicted number counts of the luminosity evolution model (Figure 13), and it is close to the flux limits of all ISOCAM deep surveys (Rowan-Robinson *et al.* 1997; Franceschini *et al.* 1996) and that of the planned WIRE survey (Hacking *et al.* 1996).

In all the three bands considered, the no evolution model (both with and without MIR features) predicts the mode of redshift distribution of galaxies with $f_\nu = 0.5$ mJy at $z \sim 0.2$–0.4. This highlights the reason why the effects of the MIR features are so weak on the number counts predicted by this model: because the high redshift galaxies never contribute significantly to the number counts, the K-correction (through which the MIR features affect number counts) is never significant.

On the other hand, the MIR features add prominent dips and bumps on the redshift distributions predicted by the density evolution model. For example the sharp peak at $z \sim 1$ on the dotted line (density evolution model) in Fig.14c ($25\mu m$) is due to the

features in in the 11 — 13μm wavelength range. This peak (after Euclidian normalization) reaches its maximum at the flux level when the 11 — 13μm features of the $L_\star$ galaxies are redshifted into the 25 μm filter ($L_\star$ does not change with redshift in the density evolution model, hence for a given flux the $L_\star$ galaxies have the same redshift). This happens at $f_{25\mu m} \sim 0.1 mJy$, and therefore a strong bump appears at this flux level on the 25 μm number counts predicted by the density evolution model (Fig.13c). At fainter flux level ($f_{25\mu m} \sim 30\mu Jy$) the bump is taken over by sources of $z \sim 2$ for which the strong emission features in the 6–8.5 μm wavelength range are in the bandpass of the WIRE 25μm camera.

In Figures 14d, 14e and 14f (no MIR features), redshift distributions predicted by the luminosity evolution model are much broader than those predicted by the density evolution model and by the no evolution model. The reason for this difference is the following: When the K-correction is insignificant, the shape of the redshift distribution is essentially determined by the product of the luminosity function and the dV/dz (c.f. Eq(25)). Thus the redshift distributions predicted both by the density evolution model and by the no evolution model resemble the 'visibility function' of a local sample (e.g. Shupe *et al.* 1998a), with a sharp peak centered at the redshift of the $L_\star$ galaxies (for the given flux). On the other hand, in the luminosity evolution model, the $L_\star$ increases rapidly with redshift, causing a much broader peak in the redshift distribution (e.g. Figure 14f). It is because of this broadness of the redshift distributions that the effects of the MIR features on the number counts predicted by the luminosity evolution model (Figure 13) are relatively weak, in particular compared to those predicted by the density evolution model (Figure 13): the effects are largely smeared out by including galaxies in a wide range of redshifts for a given flux.

5. Discussion

MIR emission features, if they exist in the IR SEDs of distant galaxies as in those of the local galaxies, can cause significant effects on the K-corrections (Figure 12), especially when the bandpass is comparable to the widths of the features (e.g. ISOCAM 15 μm and WIRE 25 μm bands). This affects the predictions on MIR number counts and the redshift distributions of different evolution models. The dips-and-bumps caused by the MIR features on the curves of the Euclidean normalized number counts will provide very useful diagnostic indicators of the type of evolution that is occurring, which may help to distinguish the density evolution model from luminosity evolution model when the redshifts are not available. On the other hand, the fluctuations in the slope of the number counts caused by the emission features should be taken into account in any attempt of determining the evolutionary rate from the *slope*.

Dramatic features are caused by the MIR features on the redshift distribution, suggesting that certain selection effects in redshift space are expected in MIR surveys. This may indeed be beneficial rather than annoying. For example, because of the strong emission features at $\sim$ 6–8 μm, the WIRE 25 μm survey may detect a large number of galaxies of $z \lesssim 3$. However, in studies on large scale structures based on deep MIR samples, these features must be separated from those caused by large scale inhomogeneities.

6. Summary and Conclusions

Our main results are summarized as follows:

1. An empirical, three-component model for the MIR SEDs of galaxies is developed. The templates of (1) a cirrus/PDR component, (2) a starburst component and (3) an AGN component are constructed from published ISO observations of MIR spectra of

galaxies. Tests show that the model can reproduce the MIR spectrum of M 82 and the ISOPHT-P 16 μm fluxes of a sample of galaxies quite well.

2. The model is applied to a sample of 1406 local galaxies ($z \leq 0.1$; Shupe et al. 1988a). Treating the K-correction as a random variable, its probability distribution (approximated by Gaussian) as a function of the redshift z and of the monochromatic luminosity L_ν are calculated for three different bandpasses (WIRE 25 μm, ISOCAM 15 μm and ISOCAM 12 μm) using these 1406 spectra.

3. Effects of MIR emission features on the MIR source counts and on the redshift distributions are studied for the same MIR bands assuming three different evolution models (no-evolution, $L \propto (1+z)^3$ and $\rho \propto (1+z)^4$). It is found that predictions by luminosity evolution model ($L \propto (1+z)^3$) and density evolution model ($\rho \propto (1+z)^4$) for source counts and redshift distributions in the WIRE 25 μm band and the ISOCAM 15 μm band are affected by the MIR emission features significantly, showing dips and bumps which can be identified as being caused by specific MIR emission features.

4. We point out that the dips-and-bumps on curves of MIR number counts will be useful indicators of evolution mode. The strong emission features at $\sim$ 6–8 μm will help the detections (especially in the WIRE 25 μm survey) of relatively high redshift ($z \sim 2$) galaxies. On the other hand determinations of the evolutionary rate based on the slope of source counts, and studies on the large scale structures using the redshift distribution of MIR sources will have to treat the effects of the MIR emission features carefully.

5. A 15 μm local luminosity function is calculated from the predicted 15 μm fluxes of the 1406 galaxies using the bivariate (15 μm vs. 25 μm luminosities) method. This luminosity function will improve our understanding of the ISOCAM 15 μm surveys.

We are grateful to James Peterson for providing the responsivity curve of WIRE 25 μm camera in electronic form. CX thanks Michael Akritas and Eric Feigelson for stimulating discussions on the Kaplan Meier estimator, and Francois-Xavier Désert for helpful comments on an earlier version of this paper. NED is supported by NASA at IPAC. This work is supported in part by a grant from NASA's Astrophysics Data Program.

REFERENCES

Acosta-Pulido, J.A., Klaas, U., Laureijs, R.J. *et al.* 1996, A&A, 315, L121.

Akritas, M.G. and LaValley, M.P. (1997), In *Handbook of Statistics, Vol. 15*, eds. G. S. Maddala and C. R. Rao, 551.

Allamandola, L.J., Tielens, A.G.G.M., Barker, J.R. 1985, ApJ, 290, L25.

Ashby, M.L.N. *et al.* 1999, in preparation.

Bothun, G.D., Lonsdale, C.J., Rice, W. 1989, ApJ, 341, 129.

Boulade, O., Sauvage, M., Altieri, B. *et al.* 1996, A&A, 315, L85.

Boulanger, F., Reach, W.T., Abergel, A. *et al.* 1996, A&A, 315, L325.

Cesarsky, D., Lequeux, J., Abergel, A. *et al.* 1996a, A&A, 315, L305.

Cesarsky, D., Lequeux, J., Abergel, A. *et al.* 1996b, A&A, 315, L309.

Clements, D. *et al.* 1998, preprint.

Cohen, M. and Volk, K. 1989, AJ, 98, 1563.

Condon, J.J. 1984, ApJ, 287, 461.

Désert, F.-X., Boulanger, F., and Puget, J.L. 1990, A&A, 237, 215.

de Grijp, M.H.K., Miley, K.K., Lub, J., and de Jong, T. 1985, Nature, 314, 240.

Fang, F., Shupe, D. L., Xu, C., and Hacking, P. B. 1998, ApJ, in press (astro-ph/9803162).

Feigelson, E. D. and Nelson, P. I. 1985, ApJ, 293, 192.

Franceschini, A., *et al.* (1997), preprint (astro-ph/9707080)

Franceschini, A., Cesarsky, C., and Rowan-Robinson, M. 1996, Memorie della Societa Astronomica Italiana.

Genzel, R., D. Lutz, E. Sturn, *et al.* 1998, ApJ, in press (in http://www.mpe-garching.mpg.de/ISO/preprint).

Giard, M., Pajot, F., Caux, E., Lamarre, J.M., and Serra, G. 1989, A&A, 215, 92.

Gillett, F.C., Kleinmann, D.E., Wright, E.L., and Capps, R.W. 1975, ApJ, 198, L65.

Giuricin, G., Madirossian, F., and Mezzutti, M. 1995, ApJ, 446, 550.

Griffiths, R.E. *et al.* 1994, ApJ, 437, 67.

Guiderdoni, B., Bouchet, F., Puget, J.-L., Lagache, G., and Hivon, E. 1997, Nature, 390, 257.

Hacking, P. B. *et al.* 1996, The Wide-Field Infrared Explorer (WIRE) Mission, to appear in International Symposium on Diffuse Infrared Radiation and the IRTS, Institute of Space and Astronomical Sciences, Sagamihara, Japan.

Hacking, P. B. *et al.* 1998, in preparation.

Hacking, P. B., Condon, J. J., and Houck, J. R. 1987, ApJ, 316, L15.

Hacking, P. B., and Soifer, B. T. 1991, ApJ, 367, L49.

Helou, G. 1986, ApJ, 311, L33.

Helou, G., Ryter, C., and Soifer, B.T. 1991, ApJ, 376, 505

Helou, G., Malhotra, S., Beichman, C.A. *et al.* 1996, A&A, 315, L157.

Kaplan, E.L. and Meier, P. 1958, *J. Am. Stat. Assoc.*, 53, 457.

Keel, W.C., de Grijp, M.H.K., Miley, K.K., and Zheng, W. 1994, A&A, 283, 791.

Koo, D.G., and Kron. R.G. 1992, ARA&A, 30, 613

Lang, K.R. 1980, Astrophysical Formulae, Springer-Verlag Berlin Heidelberg.

Léger, A. and Puget, J. L. 1984, A&A, 137, L5.

Lemke, D., Klaas, U., Abolins, J. *et al.* 1996, A&A, 315, L64.

Lu, N.Y., Helou, G., Beichman, C.A. *et al.* 1996, BAAS, 28, 1356.

Lu, N.Y, *et al.* 1998, in preparation.

Lutz, D., Genzel, R., Kuntze, D. *et al.*, 1997b, in *Extragalactic Astronomy in the Infrared*, Proceedings of the XVIIth Moriond Astrophysical Meeting, eds. G.A. Mamon, T.X. Thuan and J.T. Thanh Van; p131.

Lutz, D., Genzel, R., Sturm, E. *et al.*, 1997a, A&SS, in press (in http://www.mpe-garching.mpg.de/ISO/preprint.html).

Madau, P., Ferguson, H.C., Dickinson, M.E., Giavalisco, M., Steidel, C., and Fruchter, A. 1996, MNRAS. 283, 1388.

Maiolino, R., Ruiz, M., Rieke, G.H., and Keller, L.D. 1995, ApJ, 446, 561.

Maffei, B. 1994, thesis, "Etude des galaxies dans le domaine submillimetrique et realisation d'un spectrometre refroidi", Institut d'Astrophysique Spatiale, Univ. Paris XI.

Moorwood, A.F.M. (1986), A&A, 137, L5.

Mattila, K., Lemke, D., Haikala, L.K. *et al.* 1996, A&A, 315, L353.

Metcalfe, L., Steel, S.J., Barr, P. et al. 1996, A&A, 315, L105.

Moshir M., *et al.* 1992, IRAS Faint Source Catalog Explanatory Supplement, Version 2.

Mushotzky, R.F, and Loewenstein, M. 1997, ApJL, 481L.

Oliver, S., Goldschmidt, P., Franceschini, A., et al. 1997, MNRAS, 289, 471.

Pearson, G., and Rowan-Robinson, M. 1996, MNRAS, 283, 174.

Phillips, M.M., Aitken, D.K., and Roche, P.F. 1984, MNRAS, 207, 35.

Puget, J.L., and Léger, A.,1989, ARA&A, 27, 161.

Planesas, P., Mirabel, I.F., Sanders, D.B. 1991, ApJ, 370, 172.

Roche, P.F., Aitken, D.K., Smith, C.H., and Martin J.W. 1991, MNRAS, 248, 606.

Rowan-Robinson, M., Mann, R.G., Oliver, S.J., et al. 1997, MNRAS, 289, 490.

Rush, B., Malkan, M.A., Spinoglio, L. 1993, ApJS, 89, 1.

Schember, H., Kemp, J., Ames, H., Hacking, P., Herter, T., Fafaul, B. Everett, D., Sparr, L. 1996, "The Wide-Field Infrared Explorer (WIRE)", SPIE Proceedings, 2744, Infrared Technology and Applications XXII, p. 751-760.

Shupe, D. L., Fang, F., Hacking, P. B., and Huchra, J. P. 1998a, ApJ, in press (astro-ph/9803149).

Shupe, D.L., Larsen, M., Sargent, S., Peterson, J., Tansock, J., Luchik, T., Hacking, P., Herter, T. 1998b, in Space Telescopes V, Vol 3356, Proc. SPIE, ed. P.Y. Bely and J.B. Breckinridge (Bellingham, WA:SPIE), in press.

Soifer, B. T., and Neugebauer, G., 1991, AJ, 101, 354.

Vigroux, L., Mirabel, F., Altiéri, B. et al. 1996, A&A, 315, L93.

Verstraete, L., Puget, J.L, Falgarone, E. et al. 1996, A&A, 315, L337.

Cruikshank, D.P. and Werner, M.W. 1997, in "Planets Beyond the Solar System", ed. D.R. Soderblom, Ast. Soc. Pacific Conference Series, 119, 223.

Williams, S.E. *et al.* 1996, AJ, 112, 1335.

Xu, C. and De Zotti, G. 1989, A&A, 225, 12.

Yahil, A., Strauss, M., Davis, M., & Huchra, J. P. 1991, ApJ, 372, 380.

This manuscript was prepared with the AAS LaTeX macros v4.0.

Table 1. Local differential luminosity function at 15 μm

$\log(\nu L_\nu(15\mu m)/L_\odot)$	$\log(\phi/(\mathrm{Mpc}^{-3}\mathrm{mag}^{-1}))$	1 σ error
7.7	-2.23	-2.82
8.1	-2.88	-3.34
8.5	-2.76	-3.43
8.9	-2.88	-3.67
9.3	-3.13	-4.06
9.7	-3.52	-4.46
10.1	-4.18	-5.05
10.5	-5.06	-5.80
10.9	-5.93	-6.58
11.3	-7.00	-7.46
11.7	-7.91	-7.91

Table 2. Fitted Parameters of the 15 μm Luminosity Function

α	β	$\log(L_\star/L_\odot)$	$\log(\mathrm{C}/\mathrm{Mpc}^{-3})$
0.47 ± 0.13	2.20 ± 0.13	9.62 ± 0.15	-2.93773 ± 0.23

Fig. 1.— *Solid curve*: template of the MIR spectrum of the **cirrus/PDR** component. *Crosses with error bars*: mean ISOPHT-S spectrum of the ten FIR cold galaxies in the sample of Lu*et al.* (1998). *Dashed curve*: ISOCAM CVF spectrum of NGC 5195 (Boulade*et al.* 1996).

Fig. 2.— *Solid curve*: template of the MIR spectrum of the **starburst** component. *Crosses with error bars*: mean ISOPHT-S spectrum of of the nine FIR warm galaxies in the sample of Lu*et al.* (1997). *Dotted curve*: ISOCAM CVF spectrum of star-burst region A in Arp 244 (Vigroux*et al.* 1996).

Fig. 3.— Template of the MIR spectrum of the **AGN** component, based on the MIR spectrum of the Seyfert 2 nucleus of NGC 1068 (Lutz*et al.* 1997a). Because we are only interested in the broad band SED, the narrow emission lines are not included.

Fig. 4.— The $f_{25\mu}/f_{12\mu}$ vs. $f_{25\mu}/f_{60\mu}$ color-color diagram of the IRAS 25 μm selected sample of Shupe*et al.* (1998a). Sources with known AGNs (identified through NED) are plotted with different symbols. The rest of the sample are plotted by small dots. The dashed line marks the adopted boundary beyond which all the IR emission is considered to be due to the AGN component.

Fig. 5.— Running chart of the SED model.

Fig. 6.— Comparison between predicted (dotted curve) and observed (solid curve, taken from Lutz*et al.* 1997) MIR spectra of M 82.

Fig. 7.— Comparisons between predicted and observed (ISOPHT) 16 μm fluxes ($f_{16\mu,prt}$ and $f_{16\mu}$, respectively) for galaxies in the sample of Ashby*et al.*

Fig. 8.— Model spectra of galaxies in the sample of Ashby*et al.*, overlaid by observed flux densities (IRAS: 12 μm, 25 μm, 60 μm and 100 μm; ISOPHT: 16 μm).

Fig. 9.— Model spectra of individual galaxies in the luminosity range $9 < log(L_{25\mu}/L_{\odot}) < 10$.

Fig. 10.— The 15 μm local differential luminosity function (Table 1). The solid line is the smooth fit specified by the parameters given in Table 2.

Fig. 11.— The bandpasses of the ISOCAM 12 μm and 15 μm filters and of the WIRE 25 μm camera.

Fig. 12.— **Panel a.** The mean K_0 and the dispersion σ_K (shown by the error bars) of K-corrections of the ISOCAM 12 μm flux as functions of redshift z for galaxies in three different luminosity bins. **Panel b.** Same as Panel a. For the ISOCAM 15 μm band. **Panel c.** Same as Panel a. For the WIRE 25 μm band. **Panel d.** Dependences of K_0 and σ_K on the luminosity in the ISOCAM 12 μm band, plotted for three given redshift: $z = 0.5$, $z = 1$ and $z = 2$. **Panel e.** Same as Panel d. For the ISOCAM 15 μm band. **Panel f.** Same as Panel d. For the WIRE 25 μm band.

Fig. 13.— **Panel a.** Euclidean normalized differential counts in the ISOCAM 12 μm band, predicted by three different evolution models. **Panel b.** Same as Panel a. For the ISOCAM 15 μm band. **Panel c.** Same as Panel a. For the WIRE 25 μm band. **Panel d.** Euclidean normalized differential counts in the ISOCAM 12 μm band, predicted by evolution models otherwise identical to those in Panel a except that K-corrections are estimated from model spectra of galaxies without the MIR features. **Panel e.** Same as Panel d. For the ISOCAM 15 μm band. **Panel f.** Same as Panel d. For the WIRE 25 μm band.

Fig. 14.— **Panel a.** Redshift distributions of sources with $f_\nu = 0.5$ mJy in the ISOCAM 12 μm band predicted by the three evolution models (note that the distributions are for galaxies at this flux level, rather than for galaxies in samples brighter than this flux). **Panel b.** Same as Panel a. For the ISOCAM 15 μm band. **Panel c.** Same as Panel a. For

the WIRE 25 μm band. **Panel d.** Redshift distributions of sources with $f_\nu = 0.5$ mJy in the ISOCAM 12 μm band predicted by the evolution models otherwise identical to those in Panel a except that K-corrections are estimated from model spectra of galaxies without the MIR features. **Panel e.** Same as Panel d. For the ISOCAM 15 μm band. **Panel f.** Same as Panel d. For the WIRE 25 μm band.

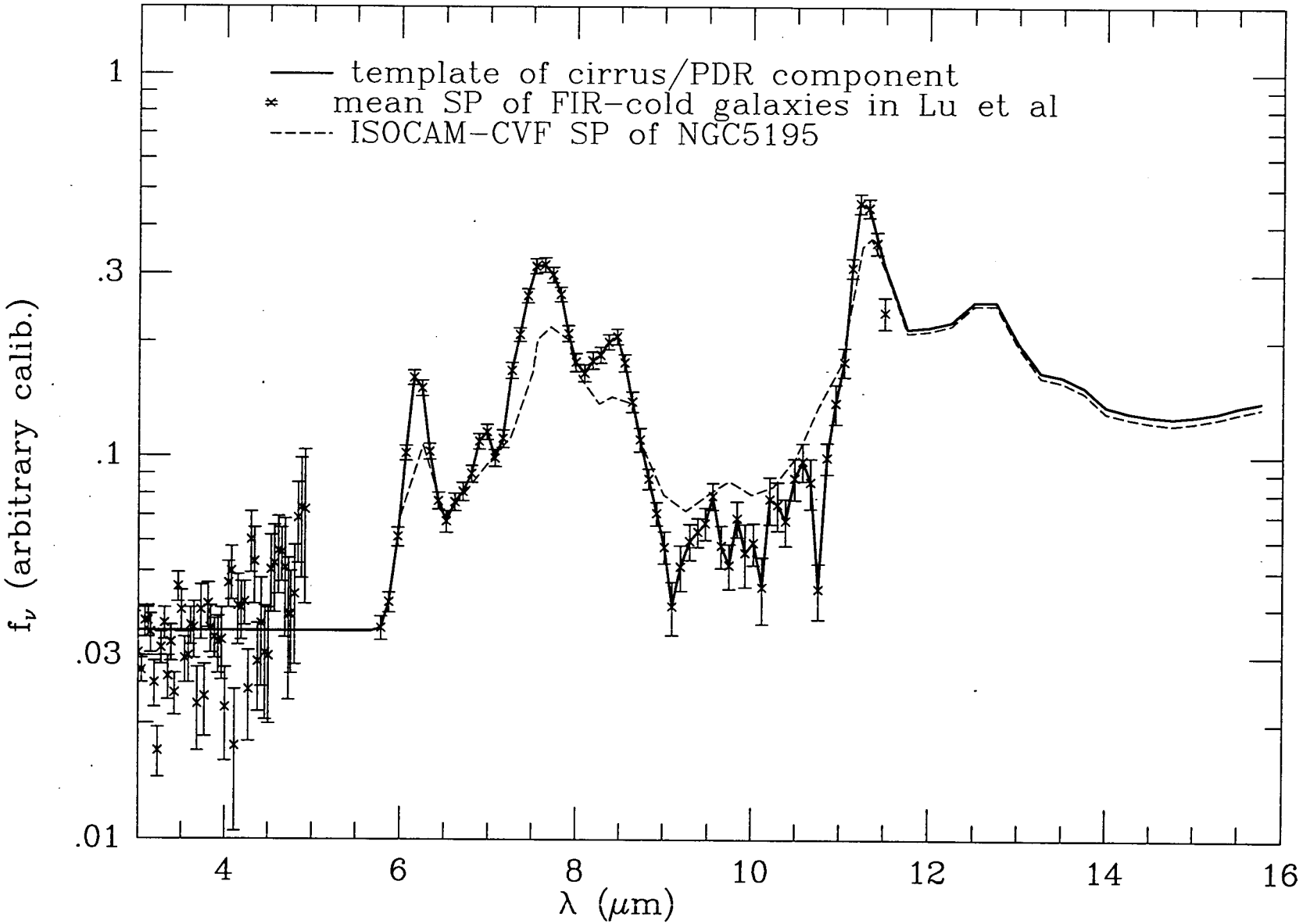
template of cirrus/PDR component
mean SP of FIR-cold galaxies in Lu et al
ISOCAM-CVF SP of NGC5195
1
.3
.1
.03
.01
f_ν (arbitrary calib.)
4
6
8
10
12
14
16
λ (μm)

Fig 1

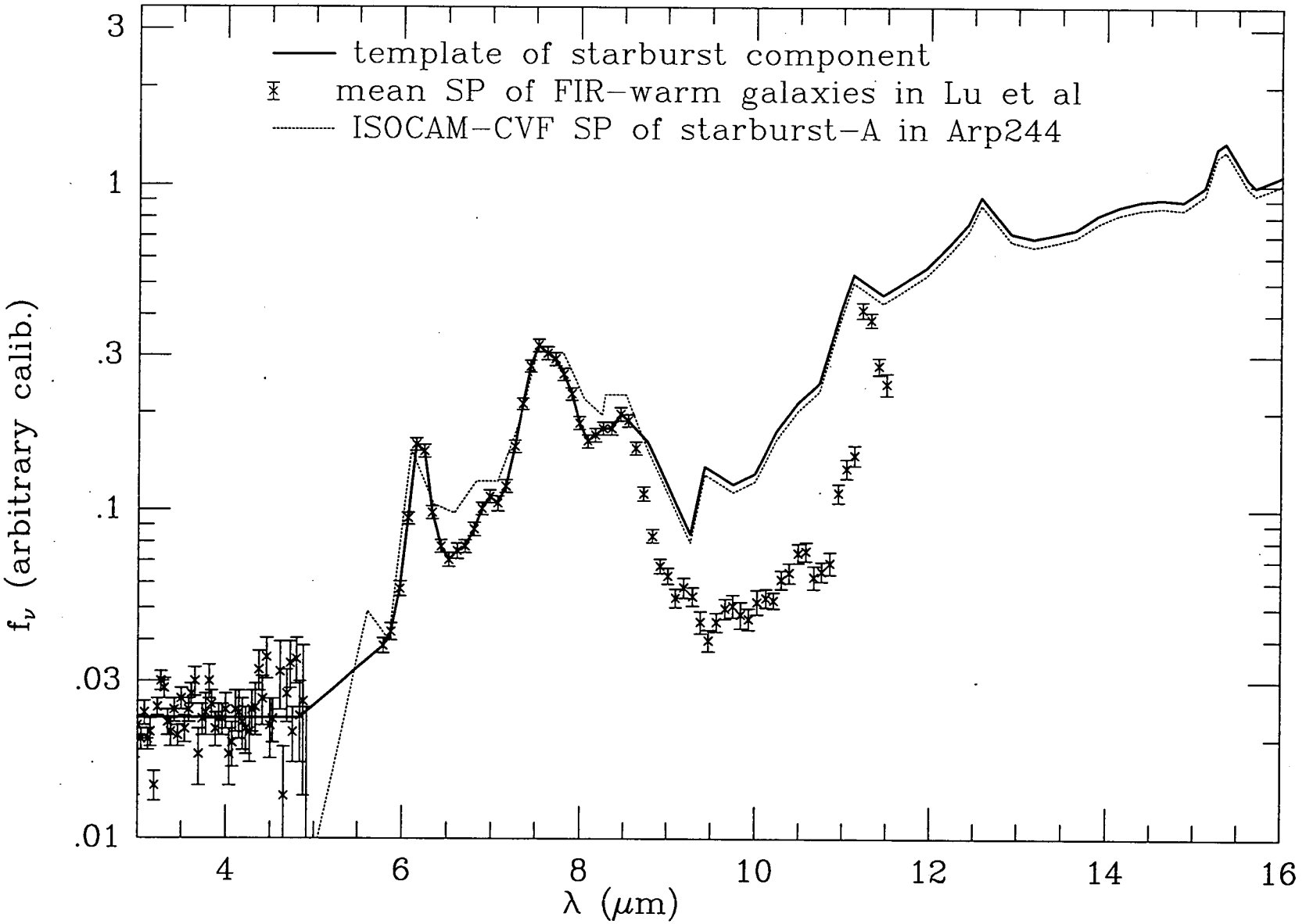
template of starburst component
mean SP of FIR-warm galaxies in Lu et al
ISOCAM-CVF SP of starburst-A in Arp244
f_ν (arbitrary calib.)
3
1
.3
.1
.03
.01
4
6
8
10
12
14
16
λ (μm)

Fig 2

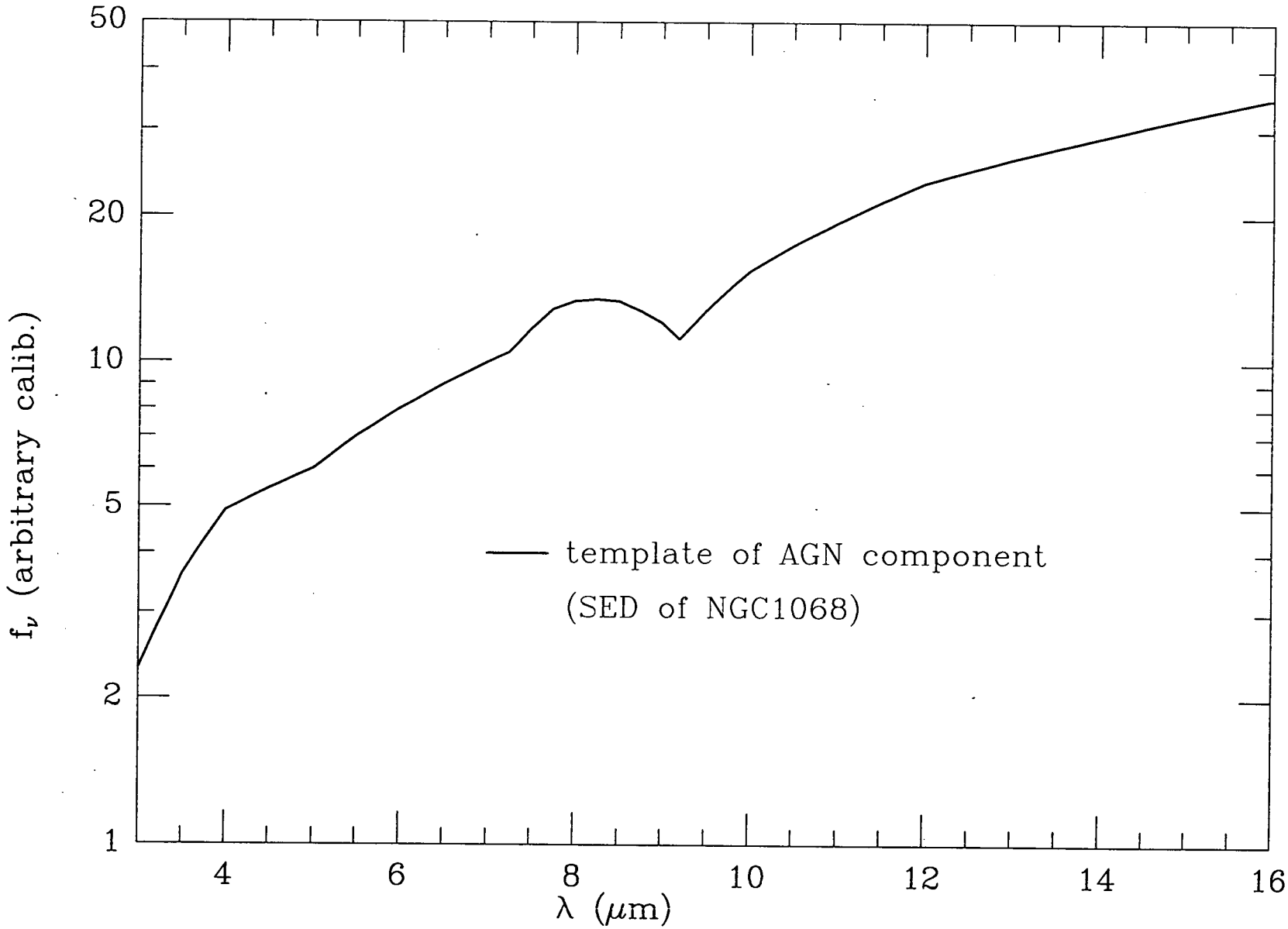
50
20
10
5
2
1
4
6
8
10
12
14
16
f_ν (arbitrary calib.)
λ (μm)
template of AGN component
(SED of NGC1068)

Fig. 3

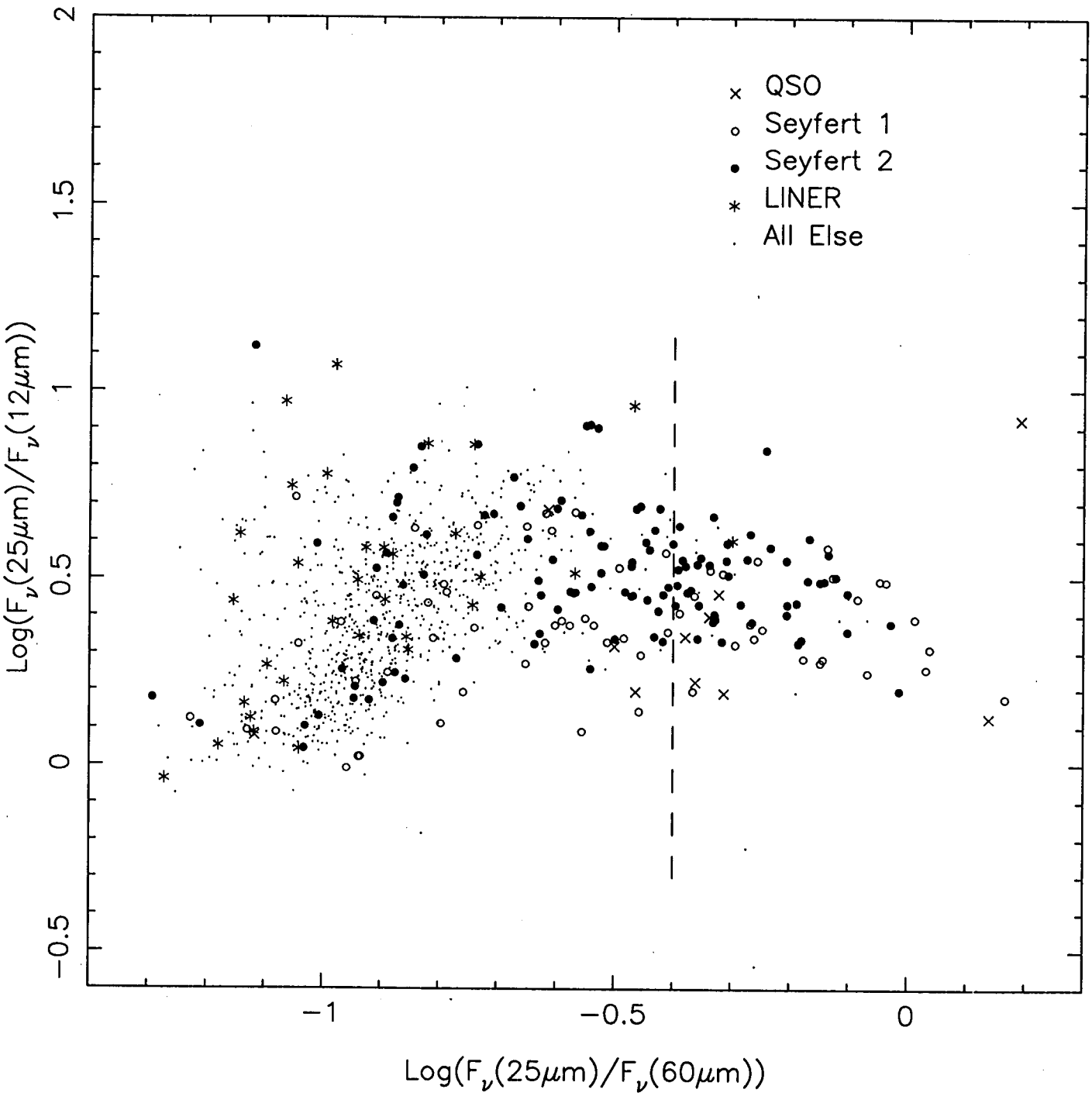
QSO
Seyfert 1
Seyfert 2
LINER
All Else
Log(F_ν(25μm)/F_ν(12μm))
Log(F_ν(25μm)/F_ν(60μm))
2
1.5
1
0.5
0
−0.5
−1
−0.5
0

Fig. 4

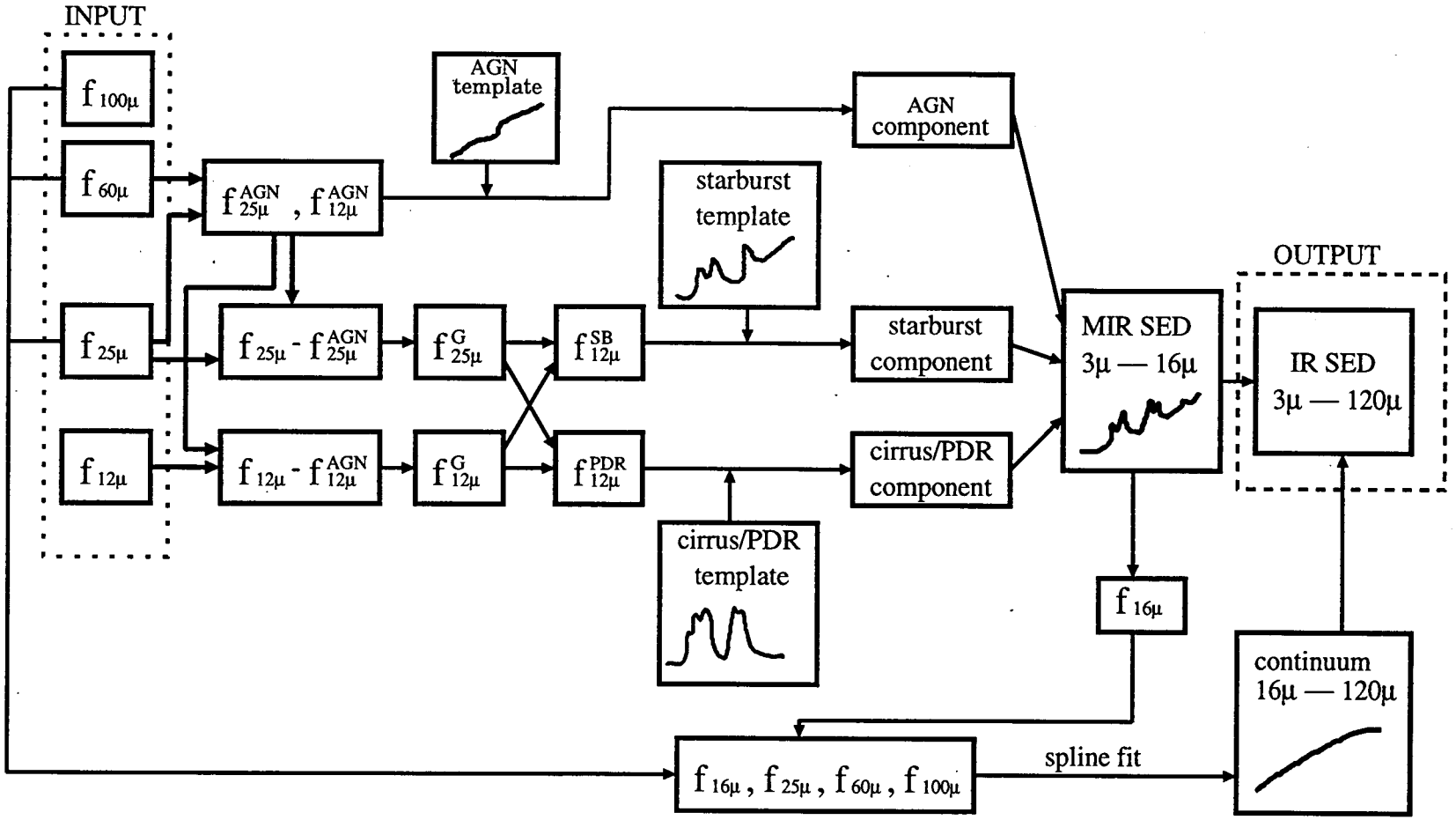
INPUT
$f_{100\mu}$
$f_{60\mu}$
$f_{25\mu}$
$f_{12\mu}$
$f^{AGN}_{25\mu}$, $f^{AGN}_{12\mu}$
AGN template
AGN component
starburst template
starburst component
$f_{25\mu} - f^{AGN}_{25\mu}$
$f^{G}_{25\mu}$
$f^{SB}_{12\mu}$
$f_{12\mu} - f^{AGN}_{12\mu}$
$f^{G}_{12\mu}$
$f^{PDR}_{12\mu}$
cirrus/PDR component
cirrus/PDR template
MIR SED 3μ — 16μ
OUTPUT
IR SED 3μ — 120μ
$f_{16\mu}$
continuum 16μ — 120μ
$f_{16\mu}$, $f_{25\mu}$, $f_{60\mu}$, $f_{100\mu}$
spline fit

Fig. 5

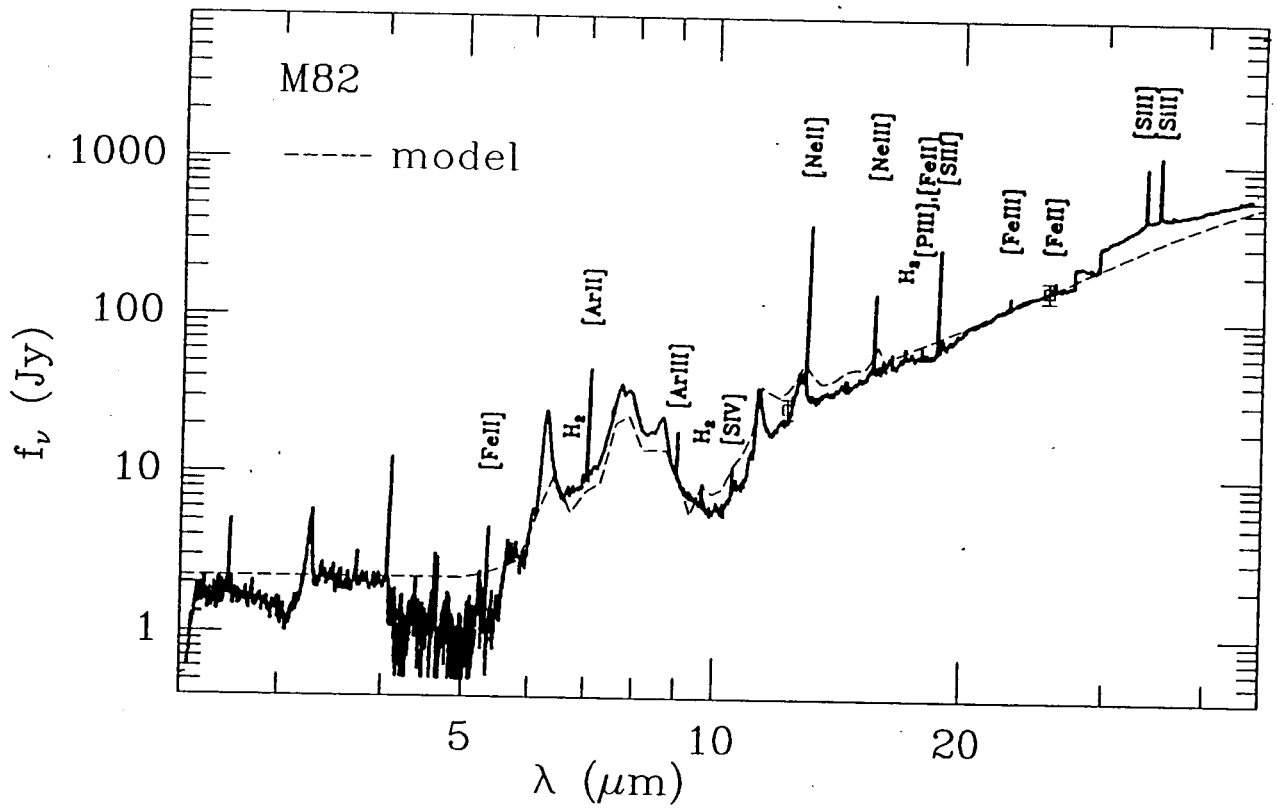
M82
----- model
1000
100
10
1
f_ν (Jy)
5
10
20
λ (μm)
[FeII]
H2
[ArII]
[ArIII]
H2
[SIV]
[NeII]
[NeIII]
H2
[PIII],[FeII]
[SiII]
[FeIII]
[FeII]
[SiII]
[SiII]

Fig. 6.

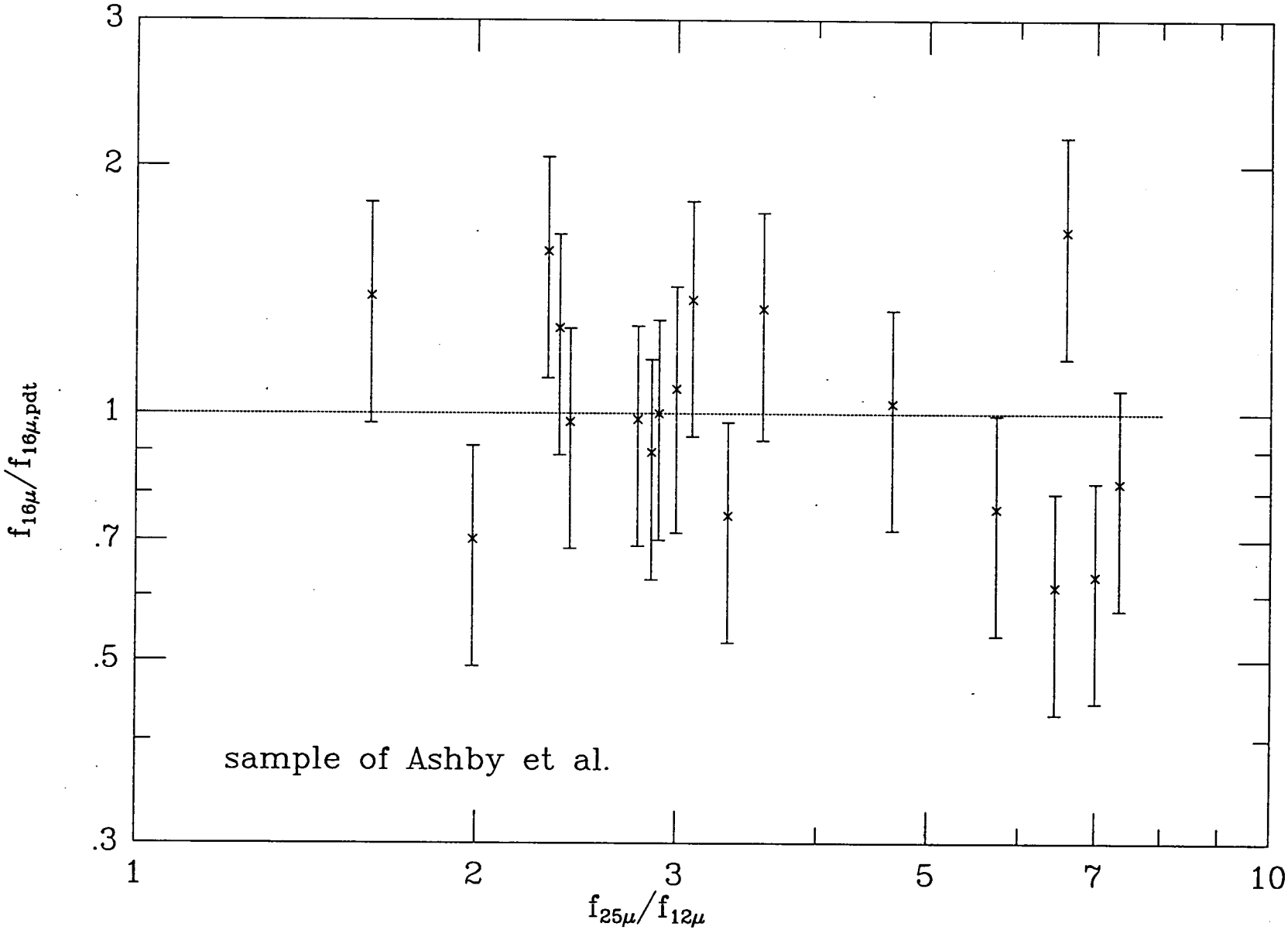
3
2
1
.7
.5
.3
1
2
3
5
7
10
$f_{16\mu}/f_{16\mu,pdt}$
$f_{25\mu}/f_{12\mu}$
sample of Ashby et al.

Fig 7

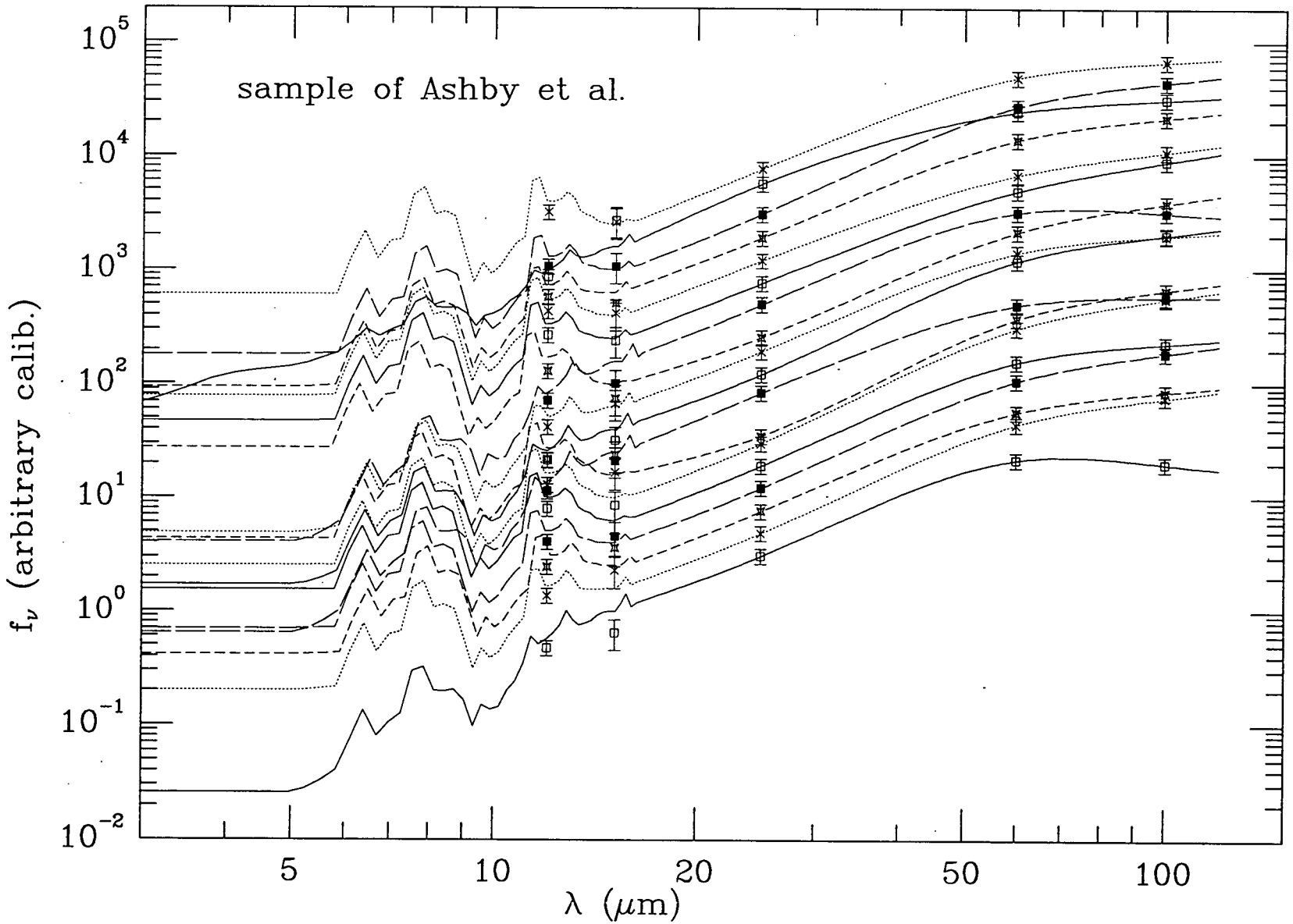
sample of Ashby et al.
f_ν (arbitrary calib.)
10^5
10^4
10^3
10^2
10^1
10^0
10^{-1}
10^{-2}
5
10
20
50
100
λ (μm)

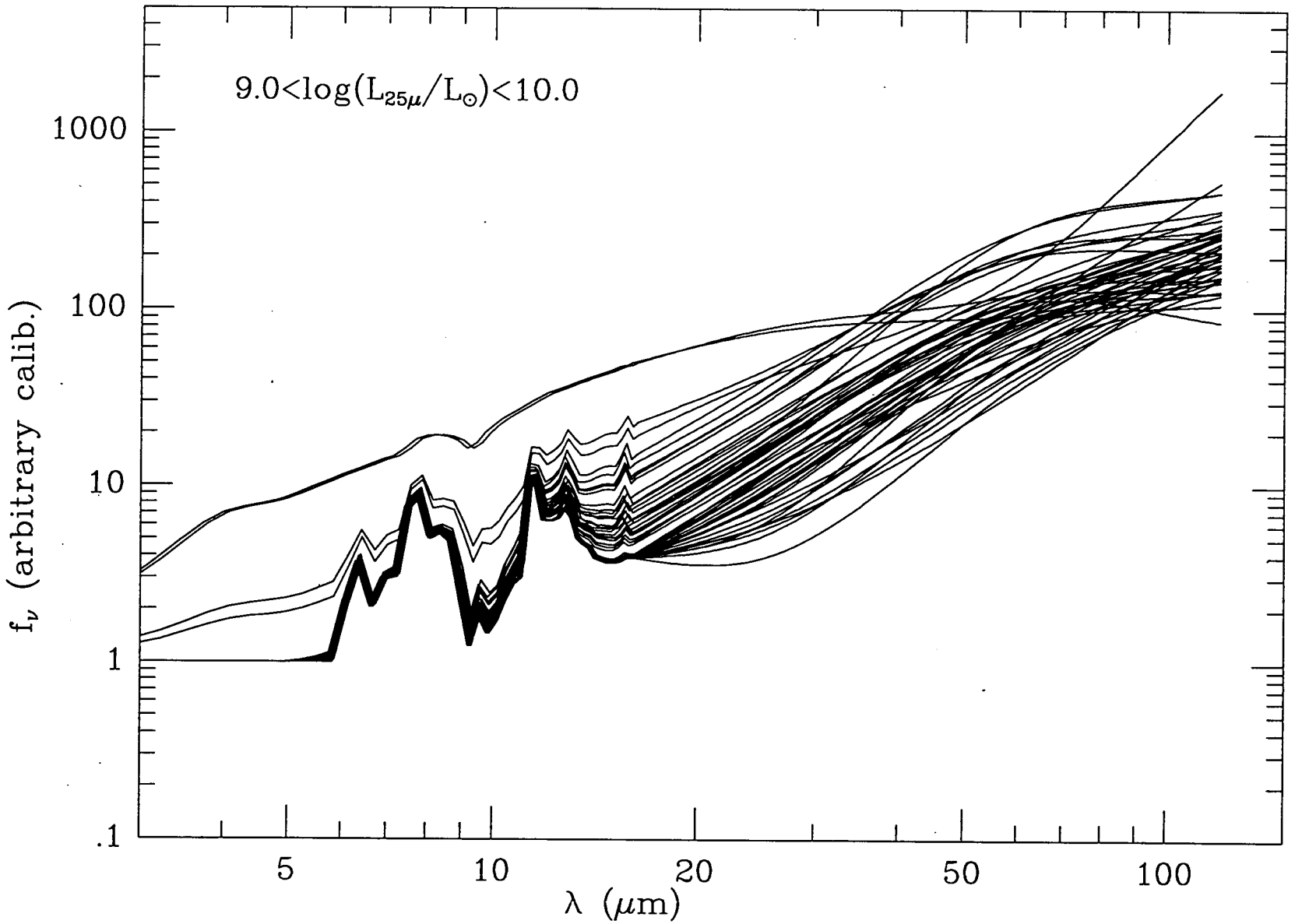
9.0<log(L25μ/L⊙)<10.0
1000
100
10
1
.1
fν (arbitrary calib.)
5
10
20
50
100
λ (μm)

Fig. 9

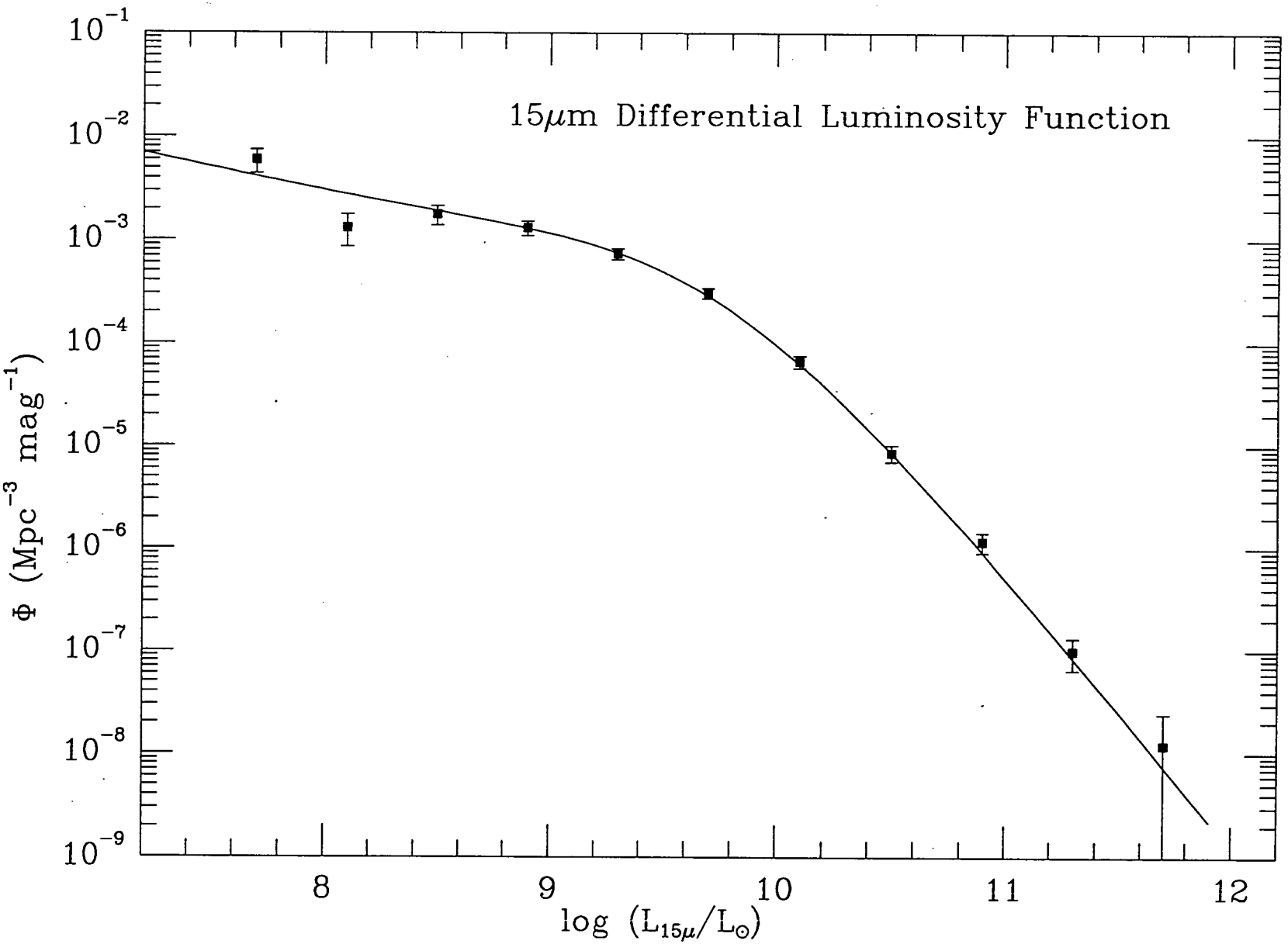
15μm Differential Luminosity Function
Φ (Mpc^{-3} mag^{-1})
10^{-1}
10^{-2}
10^{-3}
10^{-4}
10^{-5}
10^{-6}
10^{-7}
10^{-8}
10^{-9}
8
9
10
11
12
log ($L_{15\mu}/L_{\odot}$)

Fig. 19

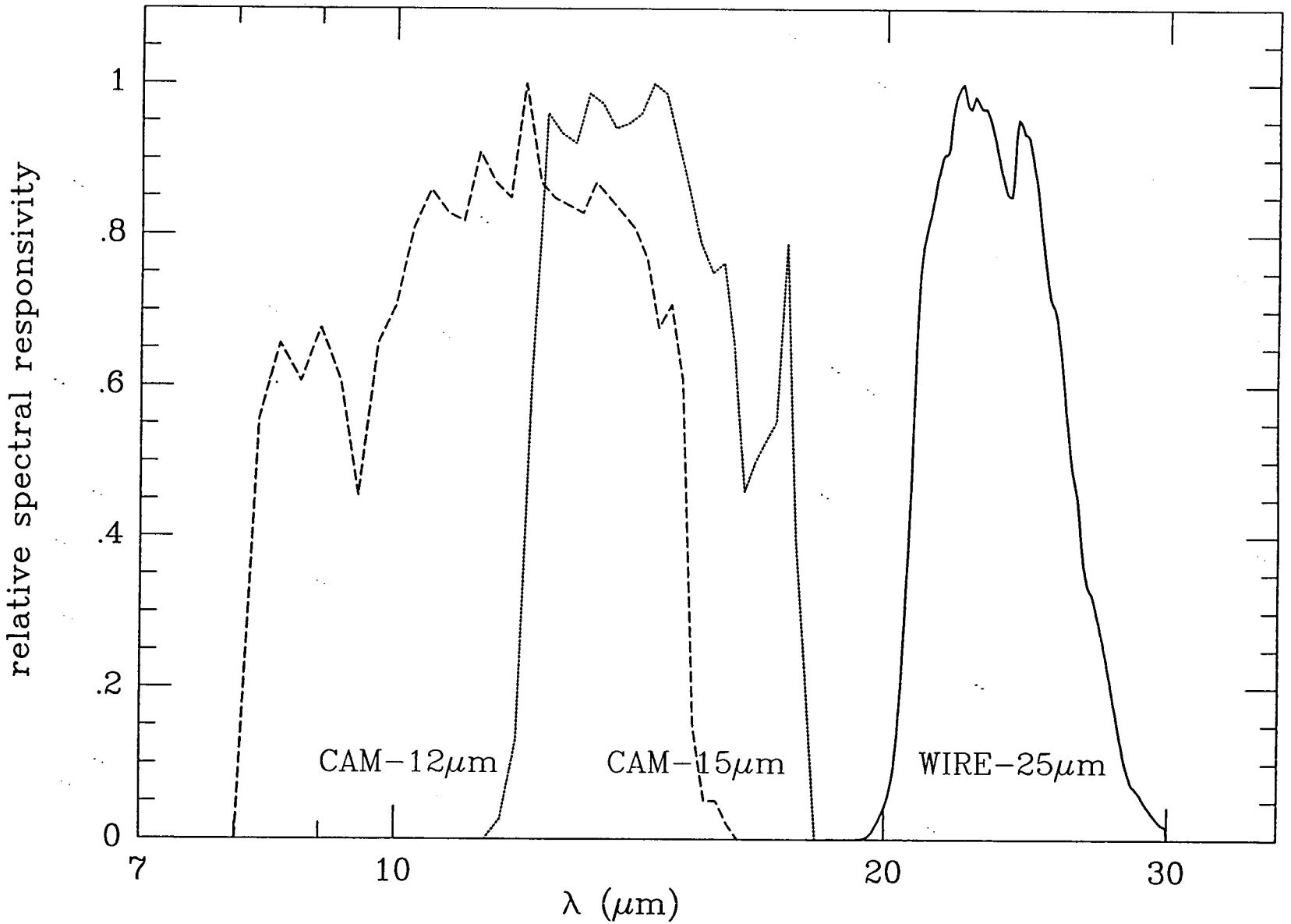
relative spectral responsivity
1
.8
.6
.4
.2
0
7
10
20
30
λ (μm)
CAM−12μm
CAM−15μm
WIRE−25μm

Fig. 11

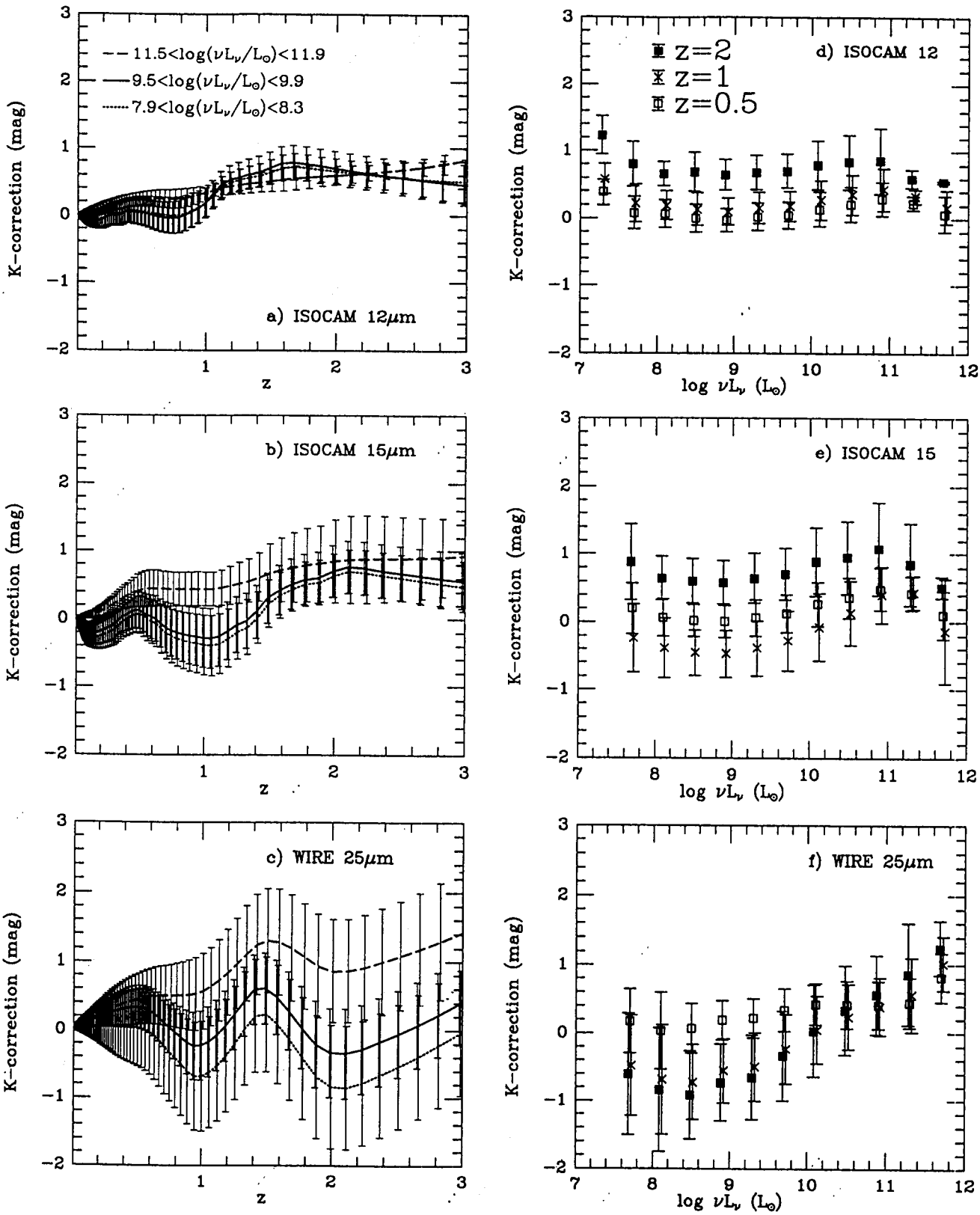
11.5<log(νL_ν/L_⊙)<11.9
9.5<log(νL_ν/L_⊙)<9.9
7.9<log(νL_ν/L_⊙)<8.3
a) ISOCAM 12μm
b) ISOCAM 15μm
c) WIRE 25μm
d) ISOCAM 12
z=2
z=1
z=0.5
e) ISOCAM 15
f) WIRE 25μm
K-correction (mag)
z
log νL_ν (L_⊙)

Fig 12

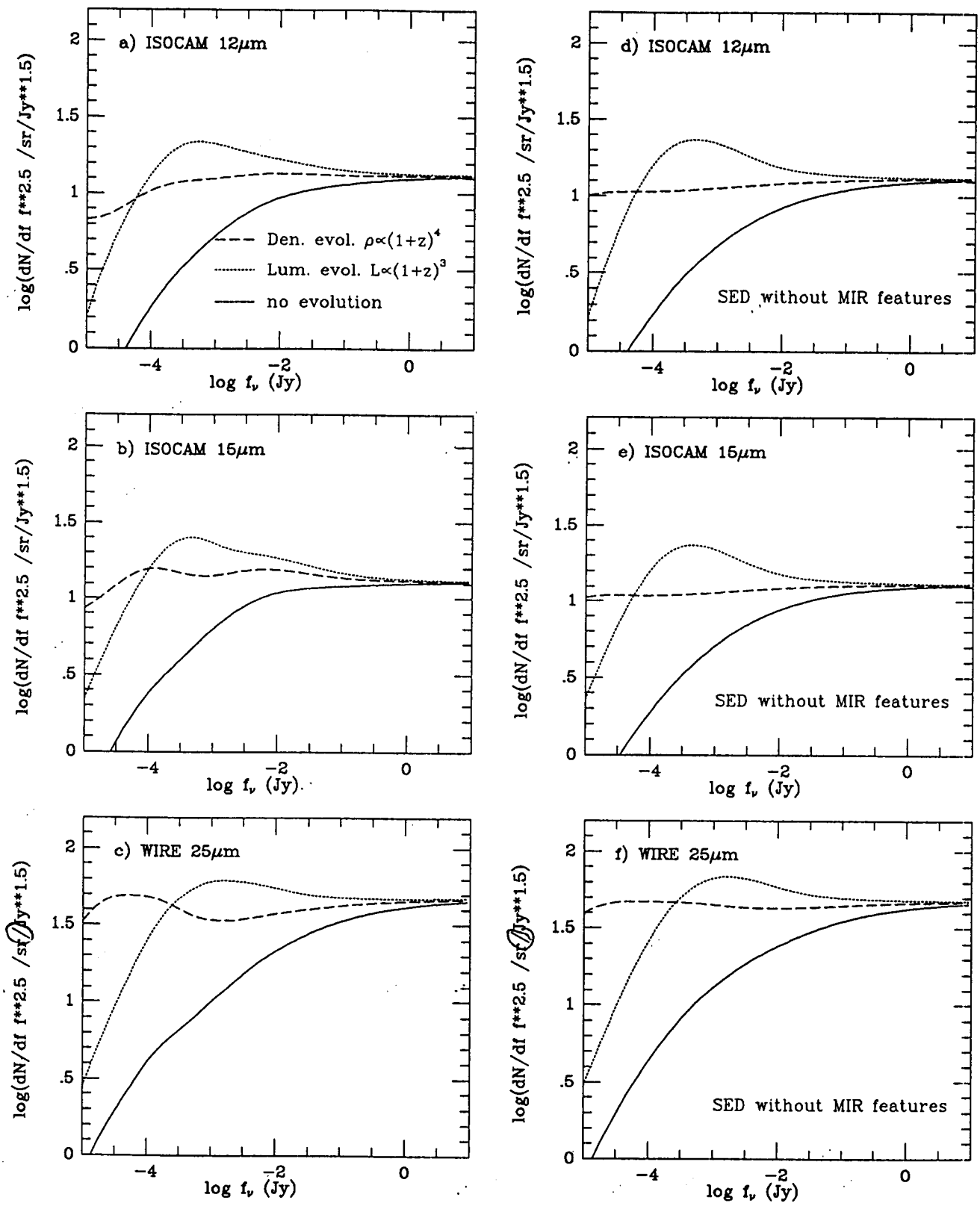
a) ISOCAM 12μm
b) ISOCAM 15μm
c) WIRE 25μm
d) ISOCAM 12μm
e) ISOCAM 15μm
f) WIRE 25μm
Den. evol. ρ∝(1+z)^4
Lum. evol. L∝(1+z)^3
no evolution
SED without MIR features
log f_ν (Jy)
log(dN/df f**2.5 /sr/Jy**1.5)

Fig. 13